J. Fluid Mech. (2009), *vol.* 641, *pp.* 389–430. © Cambridge University Press 2009
doi:10.1017/S0022112009991571

Violent breaking wave impacts. Part 2: modelling the effect of air

H. BREDMOSE[1]†‡, D. H. PEREGRINE[1]¶ AND G. N. BULLOCK[2]

[1]School of Mathematics, University of Bristol, University Walk, Bristol BS8 1TW, UK

[2]School of Engineering, University of Plymouth, Drake Circus, Plymouth PL4 8AA, UK

(Received 29 August 2008; revised 12 August 2009; accepted 12 August 2009; first published online 25 November 2009)

When an ocean wave breaks against a steep-fronted breakwater, sea wall or a similar marine structure, its impact on the structure can be very violent. This paper describes the theoretical studies that, together with field and laboratory investigations, have been carried out in order to gain a better understanding of the processes involved. The wave's approach towards a structure is modelled with classical irrotational flow to obtain the different types of impact profiles that may or may not lead to air entrapment. The subsequent impact is modelled with a novel compressible-flow model for a homogeneous mixture of incompressible liquid and ideal gas. This enables a numerical description of both trapped air pockets and the propagation of pressure shock waves through the aerated water. An exact Riemann solver is developed to permit a finite-volume solution to the flow model with smallest possible local error.

The high pressures measured during wave impacts on a breakwater are reproduced and it is shown that trapped air can be compressed to a pressure of several atmospheres. Pressure shock waves, reflected off nearby surfaces such as the seabed, can lead to pressures comparable with those of the impact. Typical examples of pressure-time histories, force and impulse are presented and discussed in terms of their practical implications. The numerical model proposed is relevant for a variety of flows where air effects are important. Further applications, including extended studies of wave impacts, are discussed.

Key words: flow–structure interactions, surface gravity waves, wave–structure interactions

1. Introduction

Numerous coastal and marine structures are damaged by wave action each year. Sometimes, even apparently well-designed breakwaters, sea defenses and vessels fail catastrophically while many other structures are left in need of extensive repair and maintenance. The damage is often caused by the violent impacts of waves that are either breaking or very close to breaking. In extreme cases, such waves can displace large caissons by several metres (Tanimoto & Takahashi 1994). Design formulae for estimating the magnitude of the impulsive pressures generated by breaking waves are presented by Goda (2000) and Oumeraci *et al.* (2001). These relationships are largely

---

† Email address for correspondence: henrik@henrikbredmose.dk

‡ Present address: DTU Mechanical Engineering, Niels Koppels Allé, Building 403, DK-2800 Kgs. Lyngby, Denmark

¶ Deceased

derived from the results of laboratory tests rather than from an in-depth analysis of the fundamental mechanics. A review of the more theoretical aspects of wave impacts on walls is provided by Peregrine (2003).

Because relatively little is known about the mechanics of breaker–structure interaction, many coastal structures are designed, at least in part, on the basis of small-scale hydraulic model tests. This introduces scale effects that are difficult to quantify. The problem is particularly acute when the wave impact involves trapped and entrained air due to the fact that air is much more compressible than water.

Bagnold (1939) was one of the first to conduct a detailed laboratory investigation into breaking-wave impacts on a vertical wall. He concluded that the highest pressures occurred when the wave trapped a small pocket of air against the wall. Hattori, Arami & Yui (1994) obtained similar results in another series of small-scale tests and noted that impulsive pressures generated in the vicinity of the still water level (SWL) travelled down through the water at the speed of sound. At full scale, Blackmore & Hewson (1984) found that none of the existing equations for estimating impact pressures agreed with their field observations. The expression they proposed broke new ground by including a coefficient related to the percentage of air entrained in the incident waves.

The vast majority of laboratory investigations are carried out using fresh water, while the waves of interest are generally in seawater. Scott (1975, 1976) was the first to demonstrate that the size of air bubbles in water is inversely related to its salinity, while Slauenwhite & Johnson (1999) found that the exudates of marine organisms have a similar effect. Because small bubbles rise through the water more slowly than large bubbles, entrained air can persist in seawater for much longer than in fresh water. Even at small scale, the resultant difference in aeration level between seawater breakers and freshwater breakers of the same size results in a tendency for the former to generate impacts of longer duration and lower peak pressure in comparison with the latter (Bullock *et al.* 2001).

The impact pressures measured at small scales are usually well below one atmosphere so that trapped and entrained air suffers relatively little compression. Conversely, at large and full scales, impact pressures of many atmospheres have been recorded (Bullock *et al.* 2004) and this can cause major reductions in air volumes. The strong dependence of the speed of sound in aerated water to the volumetric air fraction (Gibson 1970) adds another element of complexity. For example, only some 2 % by volume of air is necessary to bring the speed of sound down from the $1450\,\mathrm{m\,s^{-1}}$ in pure water to $85\,\mathrm{m\,s^{-1}}$ at atmospheric pressure. With 5 % volumetric aeration, the sound speed is $54\,\mathrm{m\,s^{-1}}$. The reduction in air volume fraction associated with large impact pressures therefore results in a local increase in sound speed. This in turn changes the way that impact pressures propagate away from the impact zone. A nonlinear feedback mechanism is thereby established between the magnitude of pressures and their speed of propagation.

Numerical models of wave impacts and slamming have been described by a number of authors. Nielsen & Mayer (2004) applied a single-phase, incompressible Navier–Stokes solver to green water slamming on ships and treated the free surface by means of the VOF (volume of fluid) technique (Hirt & Nichols 1981). Greco, Colicchio & Faltinsen (2007) coupled a boundary element method and a Navier–Stokes solver to model green-water slamming on a deck. Both the air phase and the water phase were considered incompressible. The effect of trapped air in plunging wave impacts has been modelled by Zhang, Yue & Tanizawa (1996) using an incompressible potential-flow solver for the water body and prescribing the pressure of trapped air through the ideal gas law for adiabatic compression. Faltinsen, Landrini & Greco (2004) used a similar adiabatic approach to describe the pressure in trapped air pockets beneath a floating structure. One exception from the usual assumption of incompressible flow within the water is the smoothed particle hydrodynamics (SPH) method, where artificial compressibility is introduced to allow the flow to be modelled by a number of discrete fluid particles with an appropriate interaction description. Gómez-Gesteira & Dalrymple (2004) describe how this method can be used to compute forces on a structure with vertical walls due to a dam-break flow. A promising approach for combining the two-phase flow and the VOF technique is presented in the recent study of Wemmenhove (2008), where the air phase is taken to be compressible, allowing for the modelling of trapped air pockets.

The work described in the current paper was carried out as part of an interactive field, laboratory and numerical study into Breaking Wave Impacts on steep-fronted COastal STructures (BWIMCOST). The field measurements were taken on Admiralty Breakwater, Alderney, where a masonry 'wall' steps back irregularly at a slope of 27 deg to the vertical on top of a rubble mound; see Bullock *et al.* (2003). Most of the laboratory measurements were taken in the 350 m long, 5 m wide Grosser Wellenkanal (GWK or Large Wave Channel) at the Forschungzentrum Küste (FZK or Coastal Research Centre) in Hannover, Germany, where the mound profile of the Admiralty Breakwater was reproduced at 1:4 scale with two smooth wall arrangements on top. One was a close approximation to the Admiralty Breakwater, while the other was vertical. Further details and the results from the regular wave tests have been reported by Bullock *et al.* (2007) in the first paper of this series. The current paper focuses on the design and use of a new compressible aerated-flow model that was developed to gain a better understanding of the physics of violent water-wave impacts. A prerequisite for the model was that it must accommodate the most important aeration effects observed in the GWK tests. Consequently, the model embraces numerical descriptions of both entrained air and trapped air.

In order to facilitate a qualitative comparison with the laboratory results, the numerical investigation is applied to a two-dimensional situation similar to that with the vertical wall in the GWK tests. However, because compressibility effects are important only in the immediate vicinity of the wall, where high pressures occur, the wave transformation away from the wall region is treated by an incompressible potential-flow solver. The compressible aerated-flow model is an extension of the one developed by Peregrine & Thais (1996) for a two-dimensional unsteady flow and includes an equation for energy conservation to allow for pressure shock waves. The aerated water is treated as a homogeneous mixture of incompressible liquid and adiabatically compressible gas. The numerical solution builds on the finite-volume framework 'Clawpack' (LeVeque 2002) and is based on an exact Riemann solver for the hyperbolic model equations. The results from a preliminary version of this compressible-flow model have been presented by Bredmose *et al.* (2004), Peregrine *et al.* (2004) and Peregrine *et al.* (2006).

A series of computations is presented in which an offshore wave group propagates over the mound towards the vertical wall. Impacts ranging from the flip-through type (Cooker & Peregrine 1990, 1992; Peregrine 2003), which trap no air, to overturning breakers, that trap large pockets of air, are successfully obtained by varying the initial offshore wave height. The great sensitivity of impact pressures to the incident wave conditions is apparent from the preliminary incompressible potential-flow computations. However, the main purpose of these computations is to provide input data for the compressible aerated-flow model. Results from the aerated-flow model confirm the strong sensitivity of the impact pressures to the incident wave conditions, which at least partly explains the strong variations found in the experimental results of Bullock *et al.* (2007). The numerical results also support the observation of Bagnold (1939) and Hattori *et al.* (1994) that the highest pressures occur for impacts that trap a small air pocket. As with physical measurements, the impact pressures in the vicinity of trapped air pockets exhibit the oscillatory fluctuation associated with alternate compression and expansion of the air. The computations also reveal the presence of pressure shock waves in the aerated water phase that propagate down the wall away from the impact zone. It is shown that reflection of this pressure wave from the top of the mound can lead to the generation of large pressures at the foot of the wall. An evaluation of impact forces and impulses indicates that they are less sensitive to the wave height than the maximum pressures.

The paper opens with a summary of physical characteristics of violent wave impacts as found in the GWK experiments (§ 2). The strategy for the numerical description of such violent wave impacts is presented in § 3, including the novel compressible aerated-flow model and its combined application with the incompressible potential-flow model. The numerical solution of the compressible aerated-flow model is described in § 4, together with the details of two one-dimensional validation tests. Results for violent wave impacts are given in § 5, while limitations of the computations, such as the lack of three-dimensionality, are discussed in § 6. At and near a violent impact, the flow accelerations can often exceed 100 g. This means that gravity has little influence on the local pressure field and that violent impacts in any direction between a liquid and a structure could generate similar pressure fields. The generality of the compressible aerated-flow model makes it applicable to many impact situations, not necessarily related to coastal structures, where air entrapment and/or entrainment occurs. Potential marine applications include ship slamming and flow inside LNG tankers.

2. Physical characteristics of violent wave impacts

The physical observations most directly related to the numerical study were provided by the large-scale GWK tests with a vertical wall and regular waves generated in what was essentially fresh water. Two vertical arrays of transducers were installed 1 m apart up the front of the wall. One array consisted of four pressure aeration units (PAUs), while the other consisted of nine Druck pressure transducers supplied by the FZK (the FZK units). The PAUs were specially developed by Bird *et al.* (1998) for use in both field and laboratory so that the air–water fraction or voids ratio could be estimated at locations where pressure measurements were also obtained. While the estimates were qualitative rather than quantitative, a striking feature of most of the aeration records was the way in which the voids ratio reached a minimum around the time the impact pressure reached a maximum. Even under the controlled conditions of regular waves, the impact pressures were found to be highly variable both temporally and spatially and often far from two-dimensional. The impacts associated with irregular waves also exhibited these characteristics both in the laboratory and in the field.

Despite the variability which introduced both subjectivity and overlap into the classification process, it was found that the most violent impacts could be divided into two classes termed ‘low-aeration’ and ‘high-aeration’. Schematic representations of the associated pressure-time histories can be found in Bullock *et al.* (2007, figure 4). The impacts were classed as low aeration when the PAU measurements indicated that the water contained relatively little air (typically a voids ratio $\leqslant 5\,\%$ during impact) and the main pressure spike was both high and of short duration (about 80–200 ms from initial impact till resemblance of quasi-hydrostatic pressure). In this type of

FIGURE 1. Wave impact with trapped air pocket in GWK, sloping wall. At the instant of this picture the air escapes from the pocket by bursting through the water.

impact, there was no evidence of air entrapment and it was deduced that the aeration was due to entrainment and/or entrapment of air pockets that were too small to detect individually. Impacts were classed as high-aeration when the water contained a lot of air and the main pressure spike was of a relatively long duration. In such cases, water often reached at least one of the higher transducers before it reached all of the lower transducers, which suggested that much of the increase in aeration was due to entrapment. Further evidence of either an appreciable air pocket or a dense cloud of bubbles was provided by damped oscillations in both pressure and voids ratio compatible with the alternate expansion and compression of the air following the time of peak pressure. Sub-atmospheric pressures were often recorded at the end of the first expansion phase. Pressure records similar to those described above have been recorded by many other researchers at various scales in both laboratory and field (Bagnold 1939; Blackmore & Hewson 1984; Partenscky 1988; Oumeraci, Klammer & Partenscky 1993; Hattori *et al.* 1994; Walkden *et al.* 1996) indicating that such behaviour is not specific to a particular structural geometry. Consequently, such pressure variations can be considered to be broadly generic for the breakers that generate the highest impact pressures.

There are only a few instances of successful imaging of the rapid motions associated with wave impacts, such as Chan & Melville (1988) and Hattori *et al.* (1994). In the GWK only views from above were available. However, a good impression of the experiments can be obtained from the video that is available at the electronic archive of the journal. Some indication of the violence of an impact is provided by figure 1 which, from close observation of such events, we interpret as showing the emergence of air from a trapped compressed-air pocket. From knowledge of the exposure time, we estimate that drops of water within the jet are travelling at up to $50\,\mathrm{m\,s^{-1}}$, which is an order of magnitude greater than the wave celerity.

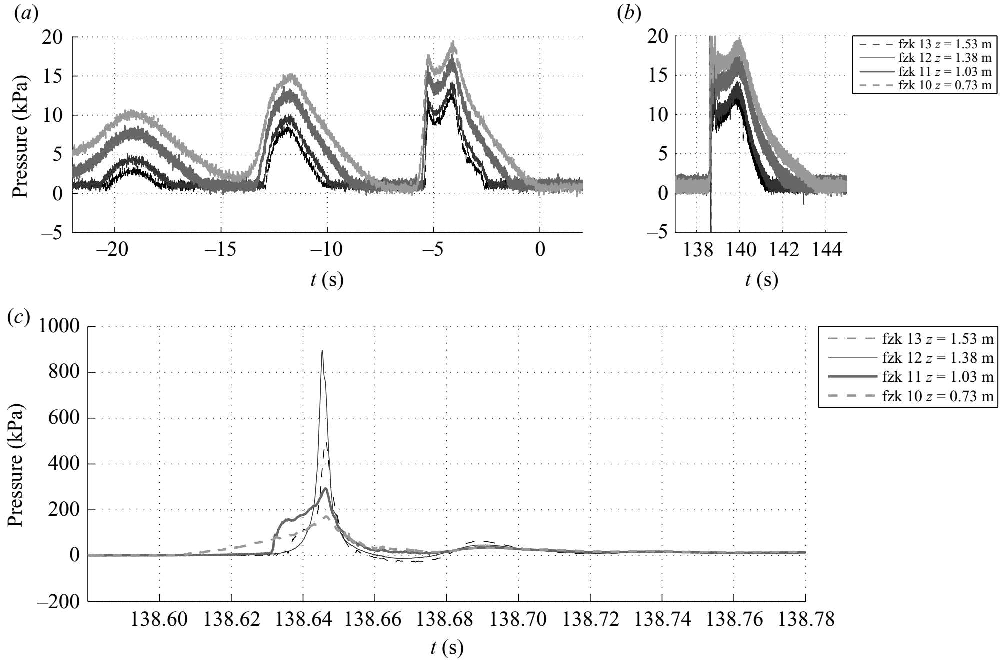

FIGURE 2. Time scales and pressure scales for (*a*) gentle waves reflecting from the wall and (*b,c*) a breaking wave generating a violent impact with entrapment of air. Note that the pressure axis of (*b*) only extends to 20 kPa. Consequently, the pressure spikes shown in (*c*) go well beyond the range of (*b*). All pressures shown are gauge pressures.

To clarify our interpretation of a 'violent impact' and to illustrate the typical magnitude and distribution of pressures measured in the GWK, figure 2 shows records from a vertical wall test with regular waves of 8 s period and a fully developed offshore height of 1.25 m. The still water depth at the wall (h) was 1.25 m, which corresponded to an offshore depth of 4.25 m at the toe of the mound. Note the different time and pressure scales of the plots. Figure 2(*a*) shows three examples of the pressures recorded shortly after the initial waves reached the wall and the height of successive waves was still increasing towards 1.25 m. In the first two, the waves were sufficiently low to simply rise up the wall without impact and were more or less totally reflected, a form of behaviour sometimes known as 'sloshing'. The third wave (centred around $t = -4$ s) was slightly steeper and the records have a characteristic double peaked structure. The initial peak corresponds to the pressure needed to accelerate water up the wall. When the water is at its maximum elevation on the wall, it is almost in free fall so that, although the crest may stretch some distance up the wall, it makes little contribution to the pressure below. The second peak corresponds to the pressure needed to decelerate the downward-falling water. We refer to this aspect of pressure plots as 'reflective pressure'.

Figure 2(*b*) shows an impact from the same test, but for a later time when the wave height was fully developed. After passing the mound, these waves were either about to break or just breaking as they reached the wall. The pressure plot can be divided into three parts. The initial 'impact pressure' (for which the full extent exceeds the vertical plotting range), an 'oscillatory pressure' characteristic of a high-aeration impact and the ‘reflective pressure’ also seen in figure 2(*a*). In engineering circles, the reflective pressure variation is often referred to as the quasi-hydrostatic phase.

The complexity of a violent impact is further illustrated by figure 2(*c*), which shows the full extent of the violent ‘impact pressure’ of figure 2(*b*) but on a much shorter time scale. Before considering this figure in detail, it is useful to recall that a 1 m depth of water generates a hydrostatic pressure of around 10 kPa and that one atmosphere is around 100 kPa. Thus, a pressure of 1 MPa corresponds to 100 m of hydrostatic pressure and 10 atmospheres. The maximum impact pressure of the current example is as much as 40 times larger than any oscillatory or reflective pressure in figure 2(*a*) and (*b*). It is these very strong impact pressures that are the subject of this paper. Note that the time span of figure 2(*c*) is 0.2 s, which is one-fortieth of a wave period.

The pressure-time series of figure 2(*c*) show many features typical for a high-aeration impact. Most notably, the pressure profiles for all four transducers show a common oscillation after the instant of maximum pressure. The two highest transducers (FZK 12 and FZK 13) show sub-atmospheric pressures after the main pressure peak. This, along with the smooth rise up to maximum pressure of FZK 12, is a clear indicator of trapped air. Simultaneous aeration measurements of the PAUs (not shown here) confirm this. The largest pressure peak (895 kPa) is measured by FZK 12, which is 1.38 m above the toe of the wall, and has a duration of less than 5 ms. FZK 11, which is 1.03 m above the toe, shows a broader peak with a maximum pressure of 294 kPa, a duration of about 20 ms and an initial pressure rise which is less smooth than for FZK12. All four signals have a maximum pressure around $t = 138.645$ s. A close inspection of the curves reveals that maximum pressure occurs first at FZK 12, with the other FZK transducers recording pressure maxima at time delays that increase with their distance from FZK 12. This indicates that the impact pressure travels away from the impact zone with finite speed.

As with most of the violent wave impacts recorded in the GWK, there were significant differences between the maximum pressures recorded by the FZK and PAU arrays of pressure transducers in the event considered above. This three-dimensionality combined with the variability in behaviour between nominally identical waves makes interpretation difficult. When also combined with the great sensitivity of the impacts to wave parameters described later in this paper, a close comparison of the physical and numerical results for particular impact events is of limited value. Given that conditions in the field are even more variable than those in the laboratory, the main value of the present numerical study is the insight provided into the fundamental physics of the process. The numerical results presented in the remainder of this paper are therefore based on representative model conditions rather than directly on measured wave data. Further details of the variability found in the laboratory may be found in Bullock *et al.* (2007).

3. Modelling strategy

The high degree of variability between the impact pressures recorded for successive waves in the GWK indicates that the impact process is highly sensitive to breaker shape. Numerous factors influence the precise shape of a particular breaker, including the bathymetry, the characteristics of the incident wave and history effects associated with the breaking, impact and reflection of previous waves. Numerical replication of specific GWK impacts would therefore require whole series of waves to be modelled in considerable detail. As the resources for this were not justified, a more computationally efficient means of gaining insight into the physical processes at work in an impact was

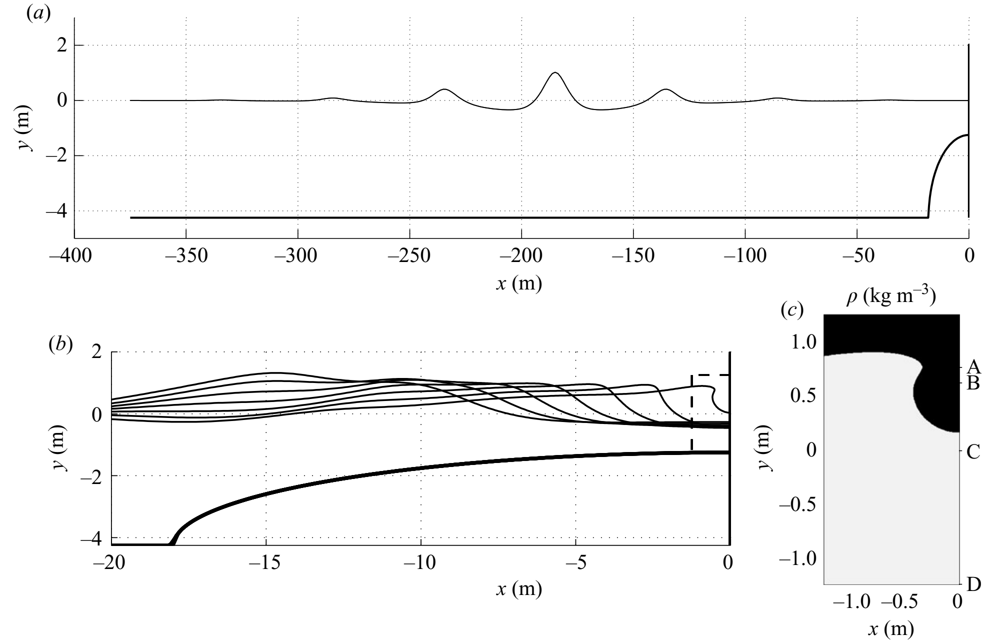

FIGURE 3. Modelling strategy. (*a*) The initial conditions for the incompressible model with a 1.45 m offshore wave height. Note the strong exaggeration of the vertical axis relative to the horizontal axis. (*b*) A computed set of free-surface profiles obtained with the incompressible model at 0.5 s intervals as the offshore wave propagates towards the wall. The dashed rectangular area adjacent to the wall denotes the domain of the compressible model. (*c*) The domain of the compressible model and the initial condition for density.

adopted. This entailed modelling a range of breaking wave conditions in circumstances similar to but not identical to those observed in the GWK with a view to obtaining knowledge that would be relevant to generic types of wave impact in both laboratory and field.

The computations presented in this paper are two-dimensional. This is probably the main limitation of the computational study as the effects of three-dimensional instabilities along the wavefront and the associated three-dimensional dynamics of air pockets are thereby precluded. However, as a first step towards an accurate numerical description of the physics of aerated wave impacts, a two-dimensional model has the advantage of simpler parameterisation and analysis of results. An extension of the study to three-dimensional is discussed in § 6.

The overall approach for the modelling is illustrated in figure 3, where the horizontal (x) and vertical (y) coordinates have origins at the wall and SWL respectively and the waves propagate in the positive x-direction. Because compressibility is of little significance until there is a strong interaction with the wall, the wave's approach to the wall is modelled by means of an incompressible two-dimensional boundary-integral method. Only the case of a vertical wall is considered and the profile of the mound is approximated by quarter of an ellipse as detailed below. The initial condition consists of an incident wave group, established by modulating a fully nonlinear regular wavetrain (Fenton 1988) as illustrated in figure 3(*a*). An example of wave transformation over the mound computed with this model is shown in figure 3(*b*). Results from the incompressible model are then used to define both the initial and driving offshore boundary conditions for a novel compressible-flow model within the region close to the wall as indicated in figure 3(*b*) and (*c*).

3.1. *Boundary-integral model for incompressible wave transformation*

The main purpose of the incompressible-flow computations is to provide initial and boundary data for the compressible-flow model. However, the incompressible results also provide insight into some of the characteristics of wave impacts as reported in § 5.

The assumption of incompressible, inviscid, irrotational two-dimensional flow permits the use of a boundary-integral formulation for a potential flow. The atmospheric pressure is taken to be constant and no surface tension effects are included. The programme used is an extension of the accurate solver for a spatially periodic domain developed by Dold & Peregrine (1986). A full description of the method may be found in Dold (1992). This model was also used by Bredmose *et al.* (2003) to compute internal sloshing in a vertically forced wave tank. The numerical approach is to discretize the free surface with Lagrangian points and time step the position and velocity potential of these points. This involves solving Laplace's equation for the normal derivative of the free surface velocity potential using a boundary-integral formulation. The accuracy of the time-integration scheme is improved by solving additionally for the first two time derivatives of the normal velocity at the free surface and utilizing the explicit Taylor expansion for the time variation of the free surface position and velocity potential. High spatial and temporal accuracy, with great computational efficiency, are further obtained by the use of high-order algorithms for the evaluation of derivatives along the fluid boundary and adaptive time stepping.

The extension to a domain bounded by uniform flow conditions is described by Tanaka *et al.* (1987). The no-flux condition through the seabed is treated by incorporating a mirror condition into the boundary-integral equations. Cooker *et al.* (1990) describe the further extension, via conformal mapping, to accommodate an obstacle on the bed. A quarter of an ellipse is used as an approximation for the shape of the mound in the GWK to gain the benefit of a simple conformal mapping. The ellipse selected as providing the best overall representation has the same height (3 m) as the experimental mound but, at 18 m long, is a metre or so shorter.

The incident waves are initiated by the numerical solution of Fenton (1988) for fully nonlinear regular waves in a constant depth of water with no net mass flux. The wavetrain is characterized by its wave height H, wavelength L and has one of its crests at $x = x_0$. A short wave group with three significant crests is produced by modulating the free surface elevation of the regular waves by the following envelope function:

$$\eta_{wavegroup} = \operatorname{sech}(k(x - x_0)/4)\eta_{regular}, \tag{3.1}$$

where $k = 2\pi/L$ is the wavenumber. The velocity potential at the free surface is treated similarly. The incident wave group shown in figure 3(*a*) is obtained with $H = 1.45$ m, $L = 50$ m, $x_0 = -185$ m and an offshore still water depth of 4.25 m. The computations presented in this paper will differ only with respect to the offshore incident wave height, H, keeping all other parameters fixed.

The computation is divided into three parts, gradually zooming into the region close to the wall with increasing resolution. Eventually, the distance between the discretization points is less than 5 mm, with time steps of less than 0.1 ms. Figure 3(*b*) shows the evolution at 0.5 s intervals of the profile of the wave illustrated in figure 3(*a*) as it shoals over the mound. Figure 3(*c*) shows the wave beginning to overturn when it is roughly 0.5 m away from the wall.

3.2. *A model for compressible aerated flow*

The compressible aerated-flow model extends the incompressible computation up to the wall and accommodates both entrapment and entrainment of air by modelling the compressibility of the air outside the water boundary and permitting a compressible air-fraction to be included within the water. This enables the flow to be followed throughout a violent impact after the wall is hit by an overturning breaking wave.

As a main assumption for the model, the aerated fluid is considered to be a homogeneous mixture of incompressible liquid (pure water) and compressible gas (air). It is also assumed that there is only one velocity field and one pressure field. The quantity β is defined as the volume fraction of air in a fluid element. The density within the gas is denoted by σ, such that $\beta\sigma$ is the overall density of gas in the fluid element. The remaining volume fraction $1-\beta$ is occupied by liquid of density M. The weighted average of density is therefore

$$\rho = \beta\sigma + (1-\beta)M, \tag{3.2}$$

where $M = 1000\,\mathrm{kg\,m^{-3}}$ is used throughout this study.

In the absence of shock waves, the compression of the air is assumed to be adiabatic and follows the ideal gas law

$$p/p_0 = (\sigma/\sigma_0)^\gamma\ . \tag{3.3}$$

Here, σ_0 and p_0 are the reference ambient air density and the atmospheric pressure, while $\gamma = 1.4$ is the adiabatic exponent of compression. We take $\sigma_0 = 1.29\,\mathrm{kg\,m^{-3}}$ and $p_0 = 10^5$ Pa throughout this study.

The possibility of pressure shock waves makes the above pressure description incomplete. To accommodate shock waves, conservation of energy must be ensured in addition to the conservation of mass and momentum (see e.g. Courant & Friedrichs 1948, § 54). This allows the entropy to increase due to a shock wave, whereas (3.3) enforces the conservation of entropy (isentropic flow). Following standard theory of gasdynamics, we consider the local energy density to be the sum of internal and kinetic energy

$$E = \rho e + \tfrac{1}{2}\rho \boldsymbol{u}\cdot\boldsymbol{u}, \tag{3.4}$$

where e is the internal energy per unit mass and $\boldsymbol{u} = (u, v)$ is the velocity vector in the Cartesian (x, y) coordinates. The internal energy per unit mass is the sum of internal energy for the gas fraction (e_g) and liquid fraction (e_ℓ) of the mixture

$$e = \frac{1}{\rho}(\beta\sigma e_g + (1-\beta)Me_\ell). \tag{3.5}$$

As the liquid is considered incompressible e_ℓ is constant, and can be set to zero without loss of generality. For an ideal polytropic gas, the internal energy is proportional to the absolute temperature T through $e_g = c_v T$, where c_v is the specific heat at constant volume. Furthermore, for an ideal gas $c_v = R/(\gamma-1)$, where R is the universal gas constant and T can be expressed from the ideal gas law $p = \sigma RT$. This leads to

$$e_g = \frac{1}{\sigma}\frac{p}{\gamma-1}, \tag{3.6}$$

which is a well-known result in gasdynamics (see e.g. Courant & Friedrichs 1948, § 3). The insertion of (3.5) and (3.6) into (3.4) now gives

$$E = \frac{\beta p}{\gamma - 1} + \frac{1}{2}\rho(u^2 + v^2) \tag{3.7}$$

for the energy density of the aerated fluid, which is consistent with the result of McCabe (2003) and reduces to the standard expression for compressible air flows for $\beta = 1$.

The flow model consists of conservation equations for mass, x-momentum, y-momentum, gas mass and energy. These are written in the conservation form as follows:

$$\rho_t + (\rho u)_x + (\rho v)_y = 0, \tag{3.8a}$$

$$(\rho u)_t + (\rho u^2 + p)_x + (\rho u v)_y = 0, \tag{3.8b}$$

$$(\rho v)_t + (\rho u v)_x + (\rho v^2 + p)_y = -\rho g, \tag{3.8c}$$

$$(\beta\sigma)_t + (\beta\sigma u)_x + (\beta\sigma v)_y = 0, \tag{3.8d}$$

$$E_t + \{(E + p)u\}_x + \{(E + p)v\}_y = -\rho g v. \tag{3.8e}$$

For $\beta \equiv 1$ (pure air), the fourth equation becomes identical to the first and the system reduces to the Euler equations of gasdynamics. For smooth (differentiable) flows where no shock waves appear, the energy conservation equation can be replaced by the explicit use of the isentropic pressure law (3.3). This is detailed in Appendix A. However, as pressure shock waves are expected for the flows to be modelled, the conservation of energy is retained in the model. For later convenience we write (3.8) in the more compact form

$$\boldsymbol{q}_t + \{\boldsymbol{F}(\boldsymbol{q})\}_x + \{\boldsymbol{G}(\boldsymbol{q})\}_y = \boldsymbol{\Psi} \tag{3.9}$$

with

$$\boldsymbol{q} = \begin{pmatrix} \rho \\ \rho u \\ \rho v \\ \beta\sigma \\ E \end{pmatrix}, \quad \boldsymbol{F} = \begin{pmatrix} \rho u \\ \rho u^2 + p \\ \rho u v \\ \beta\sigma u \\ (E + p)u \end{pmatrix}, \quad \boldsymbol{G} = \begin{pmatrix} \rho v \\ \rho u v \\ \rho v^2 + p \\ \beta\sigma v \\ (E + p)v \end{pmatrix}, \quad \boldsymbol{\Psi} = \begin{pmatrix} 0 \\ 0 \\ -\rho g \\ 0 \\ -\rho g v \end{pmatrix}. \tag{3.10}$$

This defines the state vector $\boldsymbol{q} = (\rho, \rho u, \rho v, \beta\sigma, E)$, the flux functions $(\boldsymbol{F}, \boldsymbol{G})$ in the x and y directions respectively and the source term $\boldsymbol{\Psi}$ incorporating the effects of gravity.

3.3. *Combined use of the two models*

The effects of entrained air and trapped air are expected to be significant only in regions where strong pressures occur. The compressible aerated-flow model is therefore only applied in a domain close to the wall, as indicated in figure 3(*b*). The domain is a subset of the incompressible flow domain, bounded by the vertical wall at right and the offshore and upper boundaries placed in $x = -1.25$ m and $y = 1.25$ m, respectively. The lower boundary is defined by the top of the mound, which is assumed to extend horizontally from the toe of the wall in the compressible-flow model. This simplification is justified on the basis that, even farthest from the wall on the left boundary of the compressible domain, the distance between the surface of the elliptical mound and the computational horizontal boundary is less than 0.6 % of the still water depth h. For all the computations presented in the body of this paper, the domain is discretized using a 500×1000 cell equidistant grid. This corresponds to a cell size of 2.5 mm × 2.5 mm. An analysis of the grid convergence for the numerical results shows that while the qualitative dependence of pressure and force is converged at this resolution, the converged peak pressures for the most violent impacts studied in § 5 are likely to be even larger than found on the 500×1000 cell grid. The limitations of the present grid are discussed in more detail in Appendix B.

The initial conditions for density, velocity and pressure in the compressible model are taken from output of the incompressible computations, as illustrated in figure 3(c) for the density. Due to the assumption of compressible flow within the aerated-flow model, an initial air fraction for the water phase is needed when initializing the model. This is because the liquid part of the mixture is still considered to be incompressible. For all the computations presented here, an initial aeration of 5 % was chosen. While this initial air fraction can be lowered, zero aeration cannot be chosen as this would lead to infinite sound speeds (see (4.8)) and thereby require infinitely small time steps. Although no direct measurements were taken, there is good reason to suppose that an aeration level of magnitude $O(5\,\%)$ can easily exist in water close to a structure prior to the type of impact considered here.

The free surface is initialized by a simple first-order approach in which cells with centre points inside the water phase of the incompressible-flow solution are filled with 5 % aerated water, while cells with centre points outside the water are filled with air. Because the potential-flow solution does not include the velocity field within the air, a two-step approach is taken for establishing the initial velocity field within the air. First, the compressible-flow model is run with zero velocities in the air as the initial condition, while the aerated water phase is initialized with the velocity field of the potential-flow solution. After a short time (24 ms for the computations presented here), the water motion has initiated the air motion and the water phase is re-initialized from the potential-flow solution.

The compressible model is run with impermeable, free-slip wall boundary conditions at the right boundary (vertical wall) and the bottom boundary (mound top). The offshore boundary (left) is driven by the potential-flow solution for the water phase until the incompressible model breaks down due to excessive curvature or acceleration, or because there has been a direct impact on the wall. After this time, as a first approximation, the last valid solution from the incompressible computation is simply imposed as a static inflow condition. This is considered to be acceptable because the time scale of the impacts is far smaller than the time scale of the wave motion. Within the air, a zero-gradient boundary condition is applied at the offshore boundary at all times so that the air velocity field is continuous across the boundary. A similar condition is applied at the upper boundary, except for the pressure field where the zero-gradient criterion is applied to the excess pressure in order to produce a hydrostatic pressure gradient across the boundary.

The influence of the placement of the left boundary has been checked by running an additional computation with the boundary moved 0.5 m in the offshore direction. A wave height of $H = 1.45$ m was used because it is associated with the largest impact considered in § 5. The predicted maximum pressure and force were found to decrease by 1.7 % and 1.2 % respectively. Given the strong sensitivity of the impact pressures to the wave shape detailed in § 5, these relatively small deviations were considered to be insignificant.

4. Numerical solution of the compressible aerated-flow model

The possibility of shock waves implies that it is necessary to solve the model by means of a numerical method capable of handling them. We use a second-order, finite-volume method, utilizing the Fortran package 'Clawpack' (LeVeque 2002). This finite-volume approach is based on solving Riemann problems over the numerical cell interfaces in each time step. In this context an exact Riemann solver specific for the model equations (3.8) has been developed.

To give an appropriate background for the Riemann solver theory, a brief introduction to the finite-volume method is given in § 4.1. The exact Riemann solver is presented in § § 4.2–4.6 followed by two one-dimensional validation tests of the model in § § 4.7–4.8.

4.1. *Finite-volume approach*

The model equations stated in (3.8) are the differential form of the more general statement of conservation of the state vector $\boldsymbol{q}$ within a fluid element V

$$\frac{\mathrm{d}}{\mathrm{d}t}\int_V \boldsymbol{q}\,\mathrm{d}t + \int_{\delta V}(\boldsymbol{F}n_x + \boldsymbol{G}n_y)\,\mathrm{d}s = \int_V \boldsymbol{\Psi}\,\mathrm{d}V, \tag{4.1}$$

where $(n_x, n_y) = \boldsymbol{n}$ is the outward-pointing normal vector along the boundary of V, δV. The above formulation involves no assumptions of smoothness or differentiability of $\boldsymbol{q}$ and therefore allows for both shock waves and discontinuities. Indeed, (3.8) can be obtained from (4.1) by applying the divergence theorem to the middle integral and letting V become infinitely small. However, in doing so, one has assumed the solution to be smooth and (3.8) is only valid for the subset of smooth solutions to (4.1).

The formulation (4.1) is suited to the application of a finite-volume method. We choose to solve the model on an equidistant Cartesian mesh in the (x, y)-plane with spacing Δx and Δy. Dividing (4.1) with the cell area $\Delta x \Delta y$ and integrating the flux function along the boundaries gives an equation for the cell average of $\boldsymbol{q}$, $\bar{\boldsymbol{q}} \equiv \int_V \boldsymbol{q}\,\mathrm{d}V/(\Delta x \Delta y)$,

$$\frac{\partial}{\partial t}\bar{\boldsymbol{q}}_{i,j} + \frac{1}{\Delta x}\left[F_{i+1/2,j} - F_{i-1/2,j}\right] + \frac{1}{\Delta y}\left[G_{i,j+1/2} - G_{i,j-1/2}\right] = \boldsymbol{\Psi}_{i,j}, \tag{4.2}$$

where, for example, $F_{i+1/2,j}$ denotes the flux function $\boldsymbol{F}$ from (3.10) evaluated at the interface between cell (i, j) and $(i+1, j)$. Time integration gives

$$\begin{aligned}\bar{\boldsymbol{q}}^{n+1}_{i,j} = \bar{\boldsymbol{q}}^{n}_{i,j} &- \frac{1}{\Delta x}\int_{t_n}^{t_{n+1}}\left[F_{i+1/2,j} - F_{i-1/2,j}\right]\mathrm{d}t \\ &- \frac{1}{\Delta y}\int_{t_n}^{t_{n+1}}\left[G_{i,j+1/2} - G_{i,j-1/2}\right]\mathrm{d}t + \int_{t_n}^{t_{n+1}}\boldsymbol{\Psi}_{i,j}\,\mathrm{d}t,\end{aligned} \tag{4.3}$$

which thus expresses how to update the cell average of $\bar{\boldsymbol{q}}$ in a computational cell in terms of fluxes over its boundaries.

The flux at the cell interface is obtained by solving the Riemann problem between the states at each side of the interface in every time step. The Riemann solution includes the state at the interface and thus allows a direct evaluation of the flux through (3.10). This approach, known as Godunov's method (Godunov 1959), is valid for discontinuous as well as smooth solutions and gives first-order accuracy in space for the latter case. Second-order accuracy in space is achieved by utilizing the 'waves' of the Riemann problem in combination with numerical limiters that turn off the second-order corrections in the vicinity of shocks. Specifically, the results shown in this paper make use of the 'minmod' limiter. Details of the second-order technique and limiters can be found in LeVeque (2002).

The overall time stepping of (4.2) makes use of dimensional splitting and a fractional step method for the source term. First, $\bar{\boldsymbol{q}}$ is updated through (4.2) taking only the contribution from the F-flux into account. Next, an update due to the G-flux is made and the time step is completed by an update due to contribution from the source term $\boldsymbol{\Psi}$. This type of dimensional splitting and source term splitting is called Godunov splitting and is formally only first-order accurate in time. LeVeque (2002) notes that, in practice, the error induced by Godunov splitting is often small compared with the numerical errors implied by the numerical method as a whole.

4.2. *The Riemann problem*

The basic ingredient in solving (4.2) numerically is the solution of the homogeneous one-dimensional Riemann problem for (3.8). This provides the necessary information for evaluating the numerical fluxes over the cell interfaces. The one-dimensional Riemann problem is stated as the initial value problem:

$$\begin{pmatrix} \rho \\ \rho u \\ \beta\sigma \\ E \end{pmatrix}_t + \begin{pmatrix} \rho u \\ \rho u^2 + p \\ \beta\sigma u \\ (u+p)E \end{pmatrix}_x = \begin{pmatrix} 0 \\ 0 \\ 0 \\ 0 \end{pmatrix} \tag{4.4}$$

with initial condition

$$\tilde{\boldsymbol{q}}(x,0) = \begin{cases} \tilde{\boldsymbol{q}}_L & x \leqslant 0, \\ \tilde{\boldsymbol{q}}_R & x > 0. \end{cases} \tag{4.5}$$

Here $\tilde{\boldsymbol{q}} = (\rho, \rho u, \beta\sigma, E)$ is the state vector for one-dimensional flow and $\tilde{\boldsymbol{q}}_L$ and $\tilde{\boldsymbol{q}}_R$ are two different states. The structure of the solution can be studied in terms of a local linearization of the equations

$$\tilde{\boldsymbol{q}}_t + \boldsymbol{A}\tilde{\boldsymbol{q}}_x = \boldsymbol{0}, \tag{4.6}$$

where $A_{i,j} = \partial f_i / \partial \tilde{q}_j$ is the Jacobian of the system (4.4). This matrix can be expressed in terms of $\tilde{q}_1, \ldots \tilde{q}_4$ or the primitive variables and is not shown here. For the above system $\boldsymbol{A}$ has the eigenvalues

$$\lambda_1 = u - c, \quad \lambda_2 = u, \quad \lambda_3 = u + c, \tag{4.7}$$

where

$$c = \sqrt{\frac{\gamma p}{\beta \rho}} \tag{4.8}$$

is the speed of sound and where λ_2 has multiplicity 2. This means that the solution to the initial value problem (4.5)–(4.6) consists of three waves, propagating with speeds $(u - c, u, u + c)$ away from $x = 0$. We denote the wave corresponding to λ_1 a one-wave, and likewise for the two-wave and three-wave. These waves separate regions of constant states; see figure 4. Thus, if the state in $x = 0$ is known, the flux function can be evaluated for this specific state, yielding the first-order flux for Godunov's method. Note that these waves have nothing to do with the physical water waves for which the model will later be applied. The waves discussed here in the context of the Riemann problem are local waves at the grid level, resulting from the difference in state across cell interfaces.

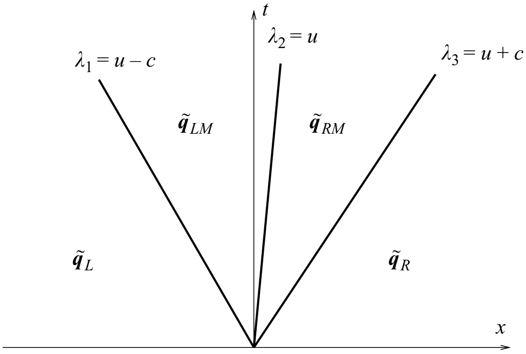

FIGURE 4. Structure of the one-dimensional Riemann problem.

It can be shown that the one-family and three-family of characteristics for the nonlinear system (4.4) are 'genuinely nonlinear', whereas the two-family is 'linearly degenerate'. In this case, the linear structure of three waves separating constant states also holds for the nonlinear system; see LeVeque (2002). The solution to the Riemann problem can then be found by connecting the initial left and right states with waves (i.e. jumps in $\tilde{\boldsymbol{q}}$) that satisfy the fully nonlinear governing equations (4.4). If the waves are smooth functions, the jump conditions can be expressed through the conservation of Riemann invariants across the waves. Alternatively, the waves may be shock waves and appropriate shock conditions must be enforced.

4.3. *Riemann invariants and shock conditions*

Consider the wave travelling with speed λ_p and introduce the travelling wave coordinate $\xi = x - \lambda_p t$. Insertion into (4.6) gives $-\lambda_p \tilde{\boldsymbol{q}}' + \boldsymbol{A}\tilde{\boldsymbol{q}}' = \boldsymbol{0}$, which is seen to hold only if

$$\tilde{\boldsymbol{q}}'(\xi) = \alpha(\xi)\boldsymbol{r}_p(\tilde{\boldsymbol{q}}(\xi)). \tag{4.9}$$

Hence, for a travelling wave solution to exist, $\tilde{\boldsymbol{q}}'(\xi)$ must be proportional to the eigenvector $\boldsymbol{r}_p$. We now look for functions $w(\tilde{\boldsymbol{q}})$ that are constant for all ξ. Such functions satisfy $(\mathrm{d}/\mathrm{d}\xi)w(\tilde{\boldsymbol{q}}(\xi)) = \boldsymbol{\nabla} w \boldsymbol{\cdot} \tilde{\boldsymbol{q}}' = \boldsymbol{0}$, which by using (4.9) yields

$$\boldsymbol{\nabla} w \boldsymbol{\cdot} \boldsymbol{r}_p = 0. \tag{4.10}$$

Hence, functions $w(\tilde{\boldsymbol{q}})$ satisfying $\boldsymbol{\nabla} w \boldsymbol{\cdot} \boldsymbol{r}_p = 0$ are constant for all ξ and are thus invariant across a p-wave. Such functions are called Riemann invariants. For the system (4.4) there are three Riemann invariants for each wave. For the one-wave, these are

$$w_{11} = \frac{\beta\sigma}{\rho}, \tag{4.11}$$

$$w_{12} = u + 2\frac{\beta c}{\gamma - 1}, \tag{4.12}$$

$$w_{13} = p/\sigma^{\gamma}, \tag{4.13}$$

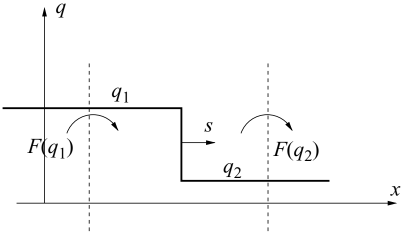

FIGURE 5. Definition sketch for derivation of the Rankine–Hugoniot conditions.

where c is given by (4.8). The conservation of w_{13} shows that the ideal gas law applies all over the one-wave. The two-wave has Riemann invariants

$$w_{21} = u, \tag{4.14}$$

$$w_{22} = p, \tag{4.15}$$

$$w_{23} = \sigma. \tag{4.16}$$

This wave is known as a contact discontinuity. It is advected with the fluid speed u and does not carry jumps in u or p. Finally, the three-wave has the Riemann invariants

$$w_{31} = \frac{\beta\sigma}{\rho}, \tag{4.17}$$

$$w_{32} = u - 2\frac{\beta c}{\gamma - 1}, \tag{4.18}$$

$$w_{33} = p/\sigma^{\gamma}, \tag{4.19}$$

which are very similar to those of the one-wave.

The one-wave and three-wave can also be shock waves. In this situation, the flow is not smooth and the differential description breaks down. Jump conditions over the waves, however, may be expressed in terms of shock conditions. Consider a shock moving with speed s from left to right; see figure 5. The conservation of each element of $\tilde{\boldsymbol{q}}$ gives $s(\tilde{\boldsymbol{q}}_2 - \tilde{\boldsymbol{q}}_1) - (\boldsymbol{F}(\tilde{\boldsymbol{q}}_2) - \boldsymbol{F}(\tilde{\boldsymbol{q}}_1)) = \boldsymbol{0}$, where, for example, $\boldsymbol{F}(\tilde{\boldsymbol{q}}_1)$ is the flux function evaluated for $\tilde{\boldsymbol{q}}$ in state one. These conditions are called the Rankine Hugoniot conditions and for the system (4.4) define four equations to be satisfied across shock waves:

$$s(\rho_2 - \rho_1) - (\rho_2 u_2 - \rho_1 u_1) = 0, \tag{4.20}$$

$$s(\rho_2 u_2 - \rho_1 u_1) - \left(\rho_2 u_2^2 + p_2 - \rho_1 u_1^2 - p_1\right) = 0, \tag{4.21}$$

$$s(\beta_2\sigma_2 - \beta_1\sigma_1) - (\beta_2\sigma_2 u_2 - \beta_1\sigma_1 u_1) = 0, \tag{4.22}$$

$$s(E_2 - E_1) - ((E_2 + p_2)u_2 - (E_1 + p_1)u_1) = 0. \tag{4.23}$$

4.4. *Solution strategy*

With known Riemann invariants and shock conditions, the Riemann problem (4.4)–(4.5) can be solved in the following way. First, an initial guess is made for the pressure in the middle state p_M. Both the pressure p and the fluid velocity u are preserved over the two-wave and are thus shared between the two middle states; see figure 4. If $p_M \leqslant p_L$, the one-wave is a rarefaction wave and conservation of the Riemann invariants (4.11)–(4.13) now gives the following formulas for the left, middle state q_{LM}:

$$\sigma_{LM} = \left(\frac{p_M}{w_{13}}\right)^{1/\gamma}, \tag{4.24}$$

$$\beta_{LM} = \frac{M w_{11}}{w_{11}(M - \sigma_{LM}) + \sigma_{LM}}, \tag{4.25}$$

$$\rho_{LM} = \frac{\beta_{LM}\sigma_{LM}}{w_{11}}, \tag{4.26}$$

$$u_M = w_{12} - \frac{2\beta_{LM}}{\gamma - 1}\sqrt{\frac{\gamma p_M}{\beta_{LM}\rho_{LM}}}. \tag{4.27}$$

Alternatively, if $p_M > p_L$, the one-wave is a shock wave and (4.20)–(4.23) can be used to calculate the left middle state:

$$s = u_L - \sqrt{\frac{(\gamma+1)\Delta p + 2\gamma p_L}{2\beta_L \rho_L}}, \tag{4.28}$$

$$\rho_{LM} = \frac{(\gamma+1)\Delta p + 2\gamma p_L}{(\gamma + 1 - 2\beta_L)\Delta p + 2\gamma p_L}\rho_L, \tag{4.29}$$

$$u_M = u_L - \Delta p\sqrt{\frac{2\beta_L}{((\gamma+1)\Delta p + 2\gamma p_L)\rho_L}}, \tag{4.30}$$

$$\beta_{LM} = \frac{(\gamma-1)\Delta p + 2\gamma p_L}{(\gamma + 1 - 2\beta_L)\Delta p + 2\gamma p_L}\beta_L, \tag{4.31}$$

$$\sigma_{LM} = \frac{(\gamma+1)\Delta p + 2\gamma p_L}{(\gamma-1)\Delta p + 2\gamma p_L}\sigma_L, \tag{4.32}$$

where $\Delta p = p_M - p_L$. Note that for $\Delta p \to 0$, the expressions simplify considerably. For example, in this limit $s \to u_L - [\gamma p_L/(\beta_L \rho_L)]^{1/2}$, which is the one-wave speed for the linearized system.

Similarly, if $p_M \leqslant p_R$, the three-wave is a rarefaction wave and $\tilde{\boldsymbol{q}}_{\mathrm{LM}}$ is given by

$$\sigma_{RM} = \left(\frac{p_M}{w_{33}}\right)^{1/\gamma}, \tag{4.33}$$

$$\beta_{RM} = \frac{M w_{31}}{w_{31}(M - \sigma_{RM}) + \sigma_{RM}}, \tag{4.34}$$

$$\rho_{RM} = \frac{\beta_{RM}\sigma_{RM}}{w_{31}}, \tag{4.35}$$

$$u_M = w_{32} + \frac{2\beta_{RM}}{\gamma - 1}\sqrt{\frac{\gamma p_M}{\beta_{RM}\rho_{RM}}}, \tag{4.36}$$

from the conservation of (4.17)–(4.19). Finally, if $p_M > p_R$, the three-wave is a shock wave and (4.20)–(4.23) give

$$s = u_R + \sqrt{\frac{-(\gamma+1)\Delta p + 2\gamma p_R}{2\beta_R \rho_R}}, \tag{4.37}$$

$$\rho_{RM} = \frac{-(\gamma+1)\Delta p + 2\gamma p_R}{-(\gamma+1-2\beta_R)\Delta p + 2\gamma p_R}\rho_R, \tag{4.38}$$

$$u_M = u_R - \Delta p \sqrt{\frac{2\beta_R}{(-(\gamma+1)\Delta p + 2\gamma p_R)\rho_R}}, \tag{4.39}$$

$$\beta_{RM} = \frac{-(\gamma-1)\Delta p + 2\gamma p_R}{-(\gamma+1-2\beta_R)\Delta p + 2\gamma p_R}\beta_R, \tag{4.40}$$

$$\sigma_{RM} = \frac{-(\gamma+1)\Delta p + 2\gamma p_R}{-(\gamma-1)\Delta p + 2\gamma p_R}\sigma_R, \tag{4.41}$$

where $\Delta p = p_R - p_M$ and with similar convergence to the solution of the linearized system for $\Delta p \to 0$.

No matter which combination of shocks or rarefactions the one-wave and three-wave possess, the above procedure gives two values for the middle fluid velocity u_M. The Riemann problem is only solved if these two velocities are identical. This provides a means of determining p_M by iteration, until the two velocities converge. The iteration is done in terms of the secant method with a starting guess of $(p_L + p_R)/2$.

4.5. *Transonic rarefaction waves*

If the magnitude of the speed of sound becomes similar to the fluid velocity, the cell interface in $x = 0$ may lie within the fan of a rarefaction wave. In this case, the Riemann solution detailed above still holds, but the state in $x = 0$ must be found using the structure of the rarefaction wave. To do this, we consider the rarefaction wave as a centred rarefaction wave, where the state values are simply functions of the similarity coordinate $\xi = x/t$,

$$\tilde{\boldsymbol{q}} = \tilde{\boldsymbol{q}}(\xi) = \tilde{\boldsymbol{q}}(x/t). \tag{4.42}$$

For a one-rarefaction wave the wave speed is $\lambda_1 = u - c$ at all points. From (4.42), we see that $\tilde{\boldsymbol{q}}$ is constant on the straight lines $x/t = \xi$ and hence $\lambda_1 = \xi$. As we are interested in the state at $x = 0$, we set $\xi = 0$, which in turn leads to $u = c$. We may use this together with conservation of the Riemann invariants (4.11)–(4.13) for a one-wave to compute the state in $x = 0$. Combining the associated equations leads to a scalar equation for ρ_0, the density at $x = 0$:

$$\left(\frac{w_{13}\gamma M}{\rho_0}\right)^{1/2} \frac{(M\rho_0 w_{11})^{\gamma/2}}{(M + (w_{11}-1)\rho_0)^{(\gamma+1)/2}} = \frac{M(\gamma-1)w_{12}}{(\gamma+1)M + 2(w_{11}-1)\rho_0}. \tag{4.43}$$

This is solved iteratively by the secant method and the remaining state variables are easily computed through the conservation of the one-Riemann invariants.

If $x = 0$ lies within the rarefaction fan of a three-wave, the condition $\lambda_3 = u + c = \xi = 0$, together with conservation of the three-Riemann invariants (4.17)–(4.19), leads to

$$\left(\frac{w_{33}\gamma M}{\rho_0}\right)^{1/2} \frac{(M\rho_0 w_{31})^{\gamma/2}}{(M + (w_{31}-1)\rho_0)^{(\gamma+1)/2}} = -\frac{M(\gamma-1)w_{32}}{(\gamma+1)M + 2(w_{31}-1)\rho_0}, \tag{4.44}$$

which is solved in the same fashion as for (4.43).

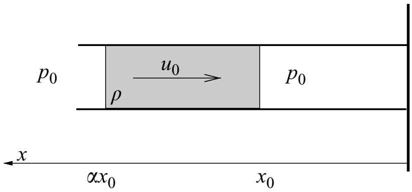

FIGURE 6. Initial condition for the piston model problem.

4.6. *The Riemann problem for two-dimensional flow*

The two-dimensional problem (4.1) is treated through dimensional splitting on a Cartesian grid. In this approach, one-dimensional Riemann problems are solved over the cell interfaces along consecutive strips of constant x and y and the solution strategy outlined above can be applied. However, when solving along an x-strip (constant y) for a two-dimensional flow, $\bar{\boldsymbol{q}}$ will contain an added component, ρv holding the momentum component in the transverse direction. It turns out, however, that jumps in v are simply advected as part of the two-wave and are left constant over both the one-wave and three-wave (see LeVeque 2002). Thus, the two-dimensional Riemann problems can be solved by using the above one-dimensional expressions and subsequently constructing the values of ρv by using the calculated values of (ρ, v_L) to the left of the two-wave and (ρ, v_R) to the right of the two-wave.

4.7. *A one-dimensional test with a trapped air pocket*

To check the aerated-flow model's ability to describe the compression of air, the model is first applied to a one-dimensional problem with a trapped air pocket. The test configuration is illustrated in figure 6, where a slug of aerated water acts like a piston and compresses a volume of air against a solid fixed wall. The wall is located at $x = 0$ and initially the air is at atmospheric pressure; the front and rear of the slug are at $x = x_0$ and $x = \alpha x_0$, respectively; the water has a uniform voids fraction of β_0; and the slug has velocity u_0. Wall boundary conditions (symmetry in $(\rho, \beta\sigma, E)$ and antisymmetry in ρu) are applied at $x = 0$ while a radiating boundary condition $(\partial\tilde{\boldsymbol{q}}/\partial x = 0)$ is imposed at the left-hand boundary at $x = x_L$.

Figure 7(*a*) shows the contour plot of pressure in the (x, t) plane resulting from a numerical solution in which $x_0 = 0.4\,\mathrm{m}$, $\alpha = 2.5$, $u_0 = 8\,\mathrm{m\,s^{-1}}$ and $\beta_0 = 0.01$. The domain was resolved with 800 computational cells, with $x_L = 1.6\,\mathrm{m}$ and the two white curves mark the front and rear trajectories of the 'water piston' as defined by the $\rho = 500\,\mathrm{kg\,m^{-3}}$ contours. The compression of the air pocket is clearly seen. Pressure oscillations can be seen inside the aerated water.

The above arrangement can also be modelled on the basis of a simple one degree of freedom system by assuming that the slug of aerated water is rigid and that the air inside the pocket has a uniform pressure and negligible velocity or acceleration. If the pocket pressure is assumed to follow the ideal gas law for adiabatic compression $p = p_0\,(x_0/x)^\gamma$, the equation of motion for the piston is

$$\rho(\alpha - 1)x_0\ddot{x} = p_0\left(\frac{x_0}{x}\right)^\gamma - p_0, \tag{4.45}$$

which can readily be rewritten as a first-order ODE system and integrated numerically by means of a standard ODE solver.

A solution for the temporal variation in pocket pressure obtained from this simple model is compared with the pressure at the wall obtained from the compressible aerated-flow model in figure 7(*b*). The striking agreement between the two sets of

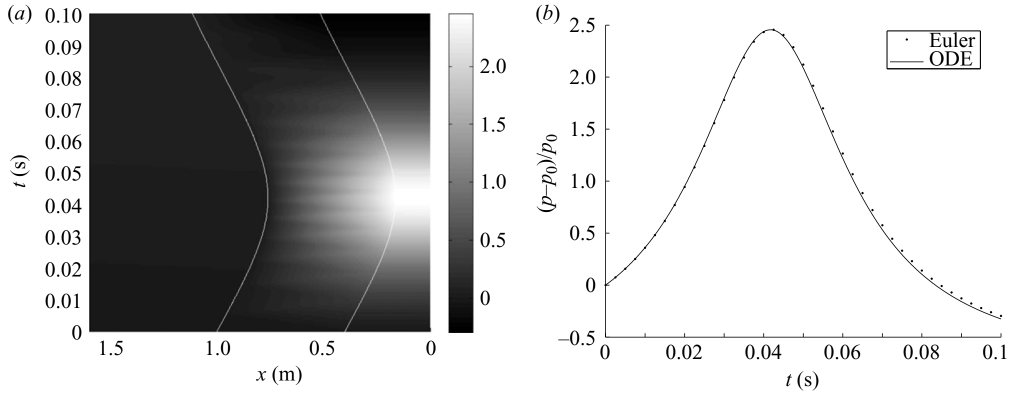

FIGURE 7. (*a*) Pressure in (x, t)-plane for one-dimensional 'water piston' test problem. The pressure unit is $(p - p_0)/p_0$ and the white curves mark the trajectory of the back and front end of the piston. (*b*) Comparison of pressure at the wall obtained by solution of the aerated-flow model and (4.45), respectively.

results indicates that the compressible aerated-flow model can accurately reproduce the main features of air entrapment situations of at least this level of complexity.

4.8. *One-dimensional tests for shock wave passing an air–water interface*

One feature of the aerated mixture modelled is the dramatic reduction of the speed of sound for intermediate values of the gas volume fraction β. This effect can be seen by combining (4.8) and (3.2) and utilizing that $M \gg \sigma$

$$c = \sqrt{\frac{\gamma p}{\beta(\beta\sigma + (1-\beta)M)}} \approx \sqrt{\frac{\gamma p}{M\beta(1-\beta)}}. \tag{4.46}$$

When a free surface is advected by the numerical model, some smearing of the air–water interface will inevitably occur. The transition from water to air will happen over a small number of grid cells, and in this transition region the speed of sound will be smaller than in the water and air phases on each side. Figure 8 presents results for two tests that were carried out to assess what happens when a pressure wave passes such a region.

Figure 8(*a*) shows results for when a pressure shock wave travels from air into water. The initial density distribution is depicted in the upper panel for a sharp interface (black line) and a smeared interface that takes up around 5 grid cells (grey line). The panels below show pressure profiles for increasing time from top to bottom. At $t = 0$ s, the pressure wave propagates towards the interface. The further snapshots show how the interaction with the interface has caused a transmitted wave to propagate into the water phase and a reflected wave to move back through the air phase. For a sharp interface, both waves are shock waves. For a smeared interface the transmitted wave has an oscillatory profile with a front amplitude greater than that of the transmitted shock wave for a sharp interface. This behaviour is due to the reduced sound speed over the smeared interface leading to a local accumulation of pressure when the initial shock wave passes through the interface. The presence of a local excess pressure excites an oscillation in the interface region and this gives the transmitted wave an oscillatory tail.

Figure 8(*b*) shows results for when a pressure shock wave travels from water into air. For a sharp interface, the wave is reflected as a rarefaction wave. The transmitted

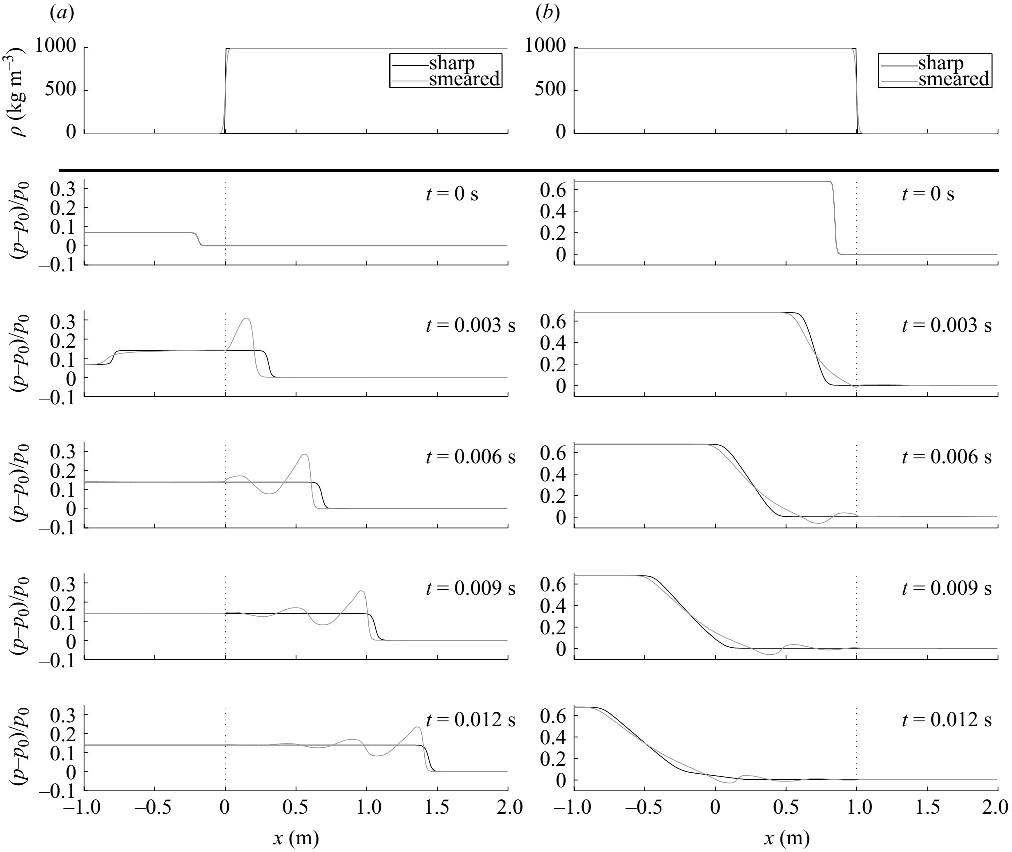

FIGURE 8. One-dimensional tests of shock wave propagation through an air–water interface. (*a*) Propagation from air into water. (*b*) Propagation from water into air. The upper plots show the initial density profile, while the lower plots show pressure profiles with time increasing in the downward direction.

wave is barely visible. In the case of a smeared interface, the reflected wave has an oscillatory tail. However, these oscillations are smaller than in the previous test and do not change the overall profile of the reflected wave to the same extent.

The above tests indicate that numerical smearing combined with the reduction in the speed of sound that occurs at intermediate gas volume fractions can lead to spurious pressure oscillations when shock waves pass the air–water interface, especially from the air side. In our computations, the air–water interface typically spans 5–10 grid cells. Grid refinement therefore helps to reduce the phenomenon, as the geometrical extent of the smeared interface is thereby reduced and the travel time through the smeared interface becomes smaller. The potential limitation of the model accuracy associated with this phenomenon, however, must be kept in mind when examining the model results.

In a real overturning breaker, the air–water interface may take the form of a layer of bubbly water. Hence, a similar behaviour due to the local reduction in sound speed may occur, although the thickness and aeration level of the layer in this case is a result of a physical process rather than numerical smearing.

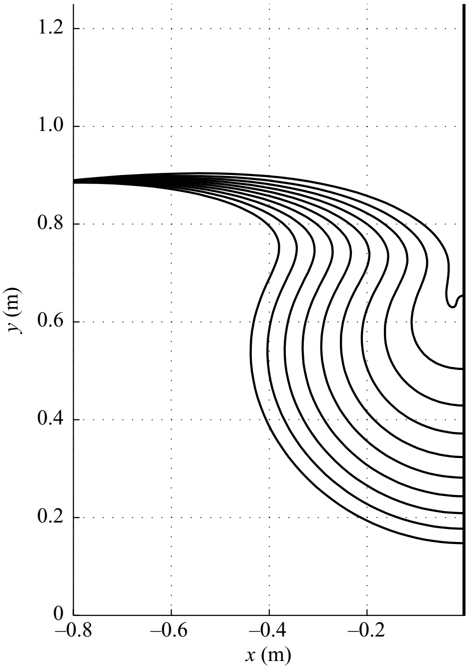

FIGURE 9. Computed surface profiles for final approach to impact for $H = 1.43$ m. The time interval between profiles is 0.005 s. The toe of the wall is at $y = -1.25$ m.

5. Numerical results for aerated wave impacts

As outlined in § 3, the aerated-flow model is driven by initial and boundary data from an incompressible potential-flow model. Although the incompressible computations neglect air effects, the results illustrate some of the important characteristics of breakers, including the way in which the shape of the free surface profile evolves up to the time of impact. This section therefore commences with a brief description of some incompressible computations (§ 5.1) before proceeding with a more detailed presentation of results from the aerated-flow model in §§ 5.2–5.5.

5.1. *Results of incompressible computations*

The incompressible computations are initiated with an offshore wave group of wave height H as described in § 3. Figure 9 shows profiles at 5 ms intervals for the final approach towards the wall for $H = 1.43$ m. Although the first couple of profiles show a crest that is beginning to overturn and seems likely to trap an air pocket against the wall, no entrapment occurs due to the fact that the trough suddenly accelerates and forms a jet that shoots up the wall. The consecutive profiles closely resemble a set of concentric quarter circles that contract towards a common centre. This indicates that all the surface particles are converging until the jet forms. Computations for this wave broke down shortly after the last profile plotted due to the strong curvature and acceleration of the free surface.

Cooker & Peregrine (1990) termed events of this type a 'flip-through' impact; see also Peregrine (2003). The name is derived from the fact that the jet up the wall 'flips' through the rapidly closing gap between the overturning crest and the wall. Thus, in a flip-through impact, the front of the wave never makes direct contact with the wall. The experimental papers of Hattori *et al.* (1994) and Lugni, Brocchini & Faltinsen

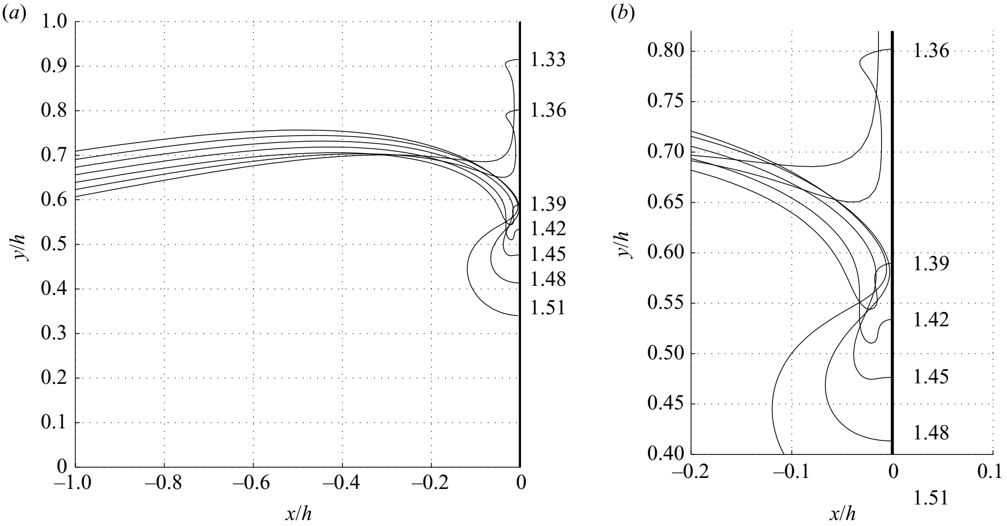

FIGURE 10. Surface profiles at the end of the incompressible-flow computations for seven different wave heights H. The toe of the wall is at $y = -1.25$ m. Each curve is labelled with the value of H in metres. (b) is a close-up of (a).

(2006) and recent experiments at University of Plymouth (Hunt-Raby, Jayaratne, Bullock & Bredmose 2008, private communication) confirm the physical existence of such impacts. In most physical situations, the conditions are not as perfect and well defined as in the numerical calculations. Consequently, the boundary between flip-through and overturning impacts, in which the crest does strike the wall, is generally somewhat blurred.

Figure 10 shows surface profiles for waves of different initial offshore wave height (H) at the time the numerical computations broke down either due to excessive surface curvature or acceleration, or because there had been a direct impact with the wall. The spatial coordinates are normalized with $h = 1.25$ m, which is the still water depth at the wall. For $H = 1.33$ m and $H = 1.36$ m, the computations are able to follow the formation and motion of the jet up the wall. However, as H increases, the crest of the wave becomes progressively more overturning. For $H = 1.48$ m and $H = 1.51$ m, the profiles indicate that a pocket of air is about to be trapped between the water and the wall. The results for $H = 1.42$ m and $H = 1.45$ m represent border-line cases where either a flip-through impact with a thin high-velocity jet will form or a tiny air pocket will be trapped. This illustrates the way in which flip-through impacts lie at the margin between reflective sloshing, in which a sheet of water runs up the wall, and overturning impacts which trap air.

The almost symmetrical contraction of the free surface in a flip-through impact implies that the flow is converging on a highly confined impact zone. High velocities are needed to take the water away from this zone, which in turn means that a large pressure gradient is required to accelerate the flow. Flip-through impacts are therefore associated with strong accelerations and large pressures. Cooker & Peregrine (1991) have reported accelerations as large as 10 000 g at the base of the jet. Figure 11 shows the variation in pressure at the point on the wall where maximum pressure occurred for offshore wave heights from 1.33 m to 1.54 m. The time variable t has its origin at the start of computation when the offshore wave group is centred at $x = -185$ m; see figure 3. Although the computations for only the two smallest wave heights are able

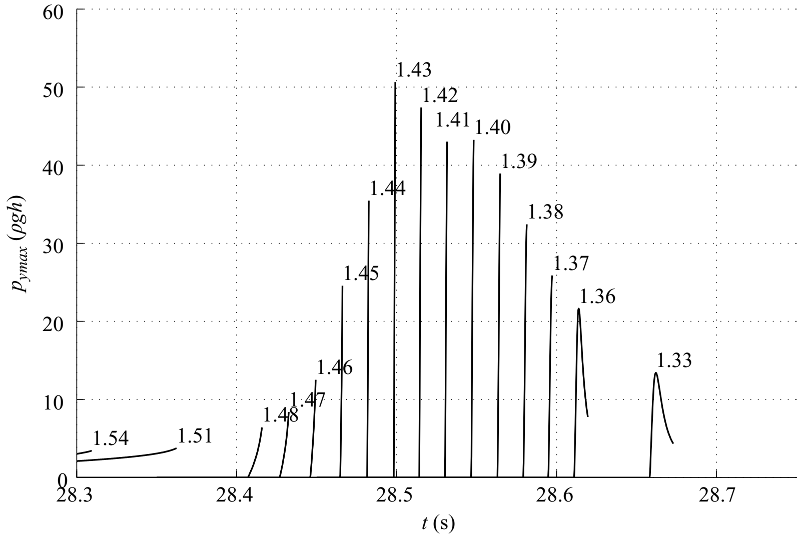

FIGURE 11. Time series for pressure on the wall at the location of maximum pressure based on incompressible potential-flow computations. Each curve is labelled with the value of H in metres.

to proceed beyond the time of maximum pressure, all the curves are characterized by a quick rise and suggest that impact pressures are highly dependent on the incident wave height. For example, changing the offshore wave height by 3 % from 1.36 m to 1.40 m leads to at least a doubling of the maximum pressure. The ratio may even be larger due to the fact that the pressure was still increasing prior to computational break down for the larger wave height. The highest pressure found was 50 ρgh.

The strong sensitivity of the impact pressures to offshore wave height is a special feature of the type of impact described above. This is in marked contrast to waves that are small enough to be well described by linear theory where reflection at a wall produces wall pressures that are only proportional to the wave height.

Further details of the pressure variation for the flip-through case of $H = 1.36$ m are given in figure 12(a), where both the pressure and the free-surface elevation on the wall are plotted in the (t, y) plane. This specific computation is chosen because it is for the largest wave height at which the maximum pressure is reached before computational breakdown. As anticipated, large pressures occur at the base of the jet. The time of maximum pressure is almost identical for all elevations on the wall. A close-up of the region of maximum pressure is shown in figure 12(b) with a maximum pressure of 21.6 ρgh. Given that figure 12(b) covers a time interval of only 15 ms, which is 1/500th of the wave period, it is apparent that the extreme pressures are of very short duration.

The incompressible calculations presented here indicate that, under the conditions considered in this paper, as H increases the first violent impacts will be of the flip-through type with little or no air entrapment. They also suggest that flip-through impacts occur for a narrow band of wave conditions between sloshing and overturning impacts.

Because the incompressible model is not able to cope with impacts of overturning waves, further investigation into the characteristics of violent wave impacts has been

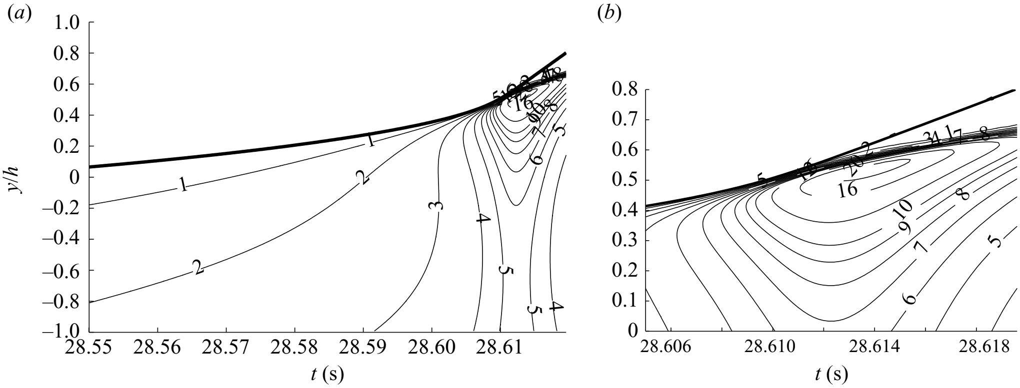

FIGURE 12. (*a*) Contour plot of wall pressure as a function of time for $H = 1.36\,\text{m}$. The position of the free surface at the wall is shown by a thick curve. The isolines give the pressure values in ρgh. (*b*) Close-up of (*a*) showing region of maximum pressure.

carried out using the compressible aerated-flow model that can handle such situations together with the associated effects of entrained and entrapped air. The compressible model also takes account of the air flow around the impacting wave and this might affect the water motion even in cases where no air is trapped. As explained in § 3, input data for the compressible model are provided by the incompressible model. Consequently, the results presented below are continuations of the incompressible results.

5.2. *Flip-through impact (compressible computations)*

The first compressible results considered are for $H = 1.36\,\text{m}$. The incompressible computations for this offshore wave height led to a classic flip-through impact and were discussed in § 5.1. The new results for the variation in density and pressure are presented in figure 13. Figure 13(*a, b*) shows the snapshots of the density and pressure fields, while figure 13(*c, d*) shows the temporal evolution of pressure on the wall. A detailed description of figure 13(*a–d*) is given in the caption. To facilitate a direct comparison of results for different values of H, one fixed grey scale has been adopted for all the pressure contour plots in figures 13, 15–18. Because the pressures are relatively low, this causes the contour plots in figure 13 to be rather dark.

The snapshots in the first column show the wavefront as it approaches the wall. The preceding trough is already moving upwards and reducing the apparent wave height. The second column is for the time instant just before the largest pressure of 17.9 ρgh occurs and shows the early stages of jet formation together with the associated strong pressure at the base of the jet. The remaining two columns illustrate how the jet develops. Throughout this time, high pressures propagate away from the impact zone as a pressure wave with an almost semicircular front. When the pressure wave reaches the top of the impermeable mound (lower boundary), it is reflected giving rise to substantial bed pressures of up to 7 ρgh. The downward propagation of the impact pressure is illustrated in the lower panel of the figure which shows the reflection of the pressure wave together with its subsequent upward propagation in the (t, y) plane.

Free surface profiles from the compressible and incompressible computations are compared in figure 14. The density field of the compressible computation is shown in

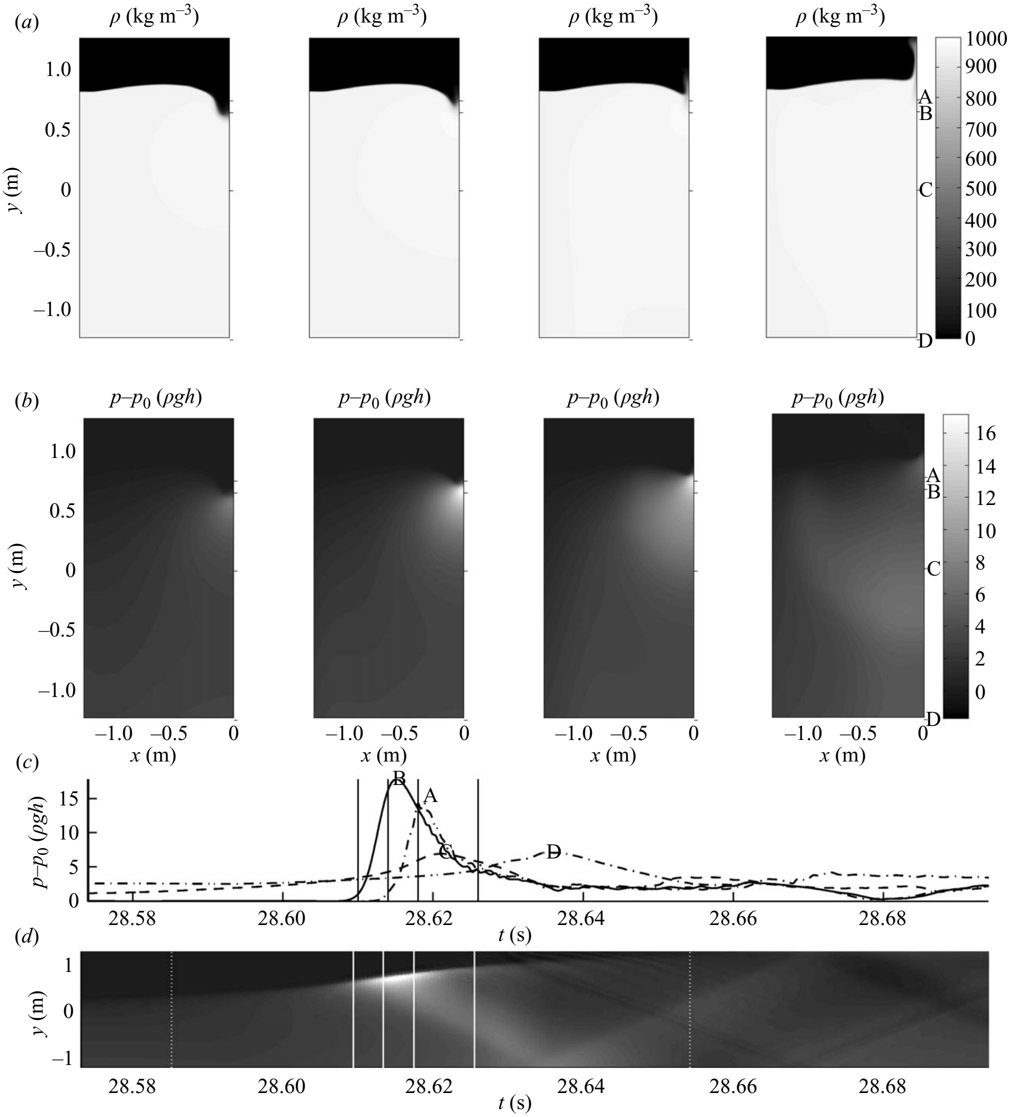

FIGURE 13. Density and pressure variation during the flip-through impact with $H = 1.36$ m. (*a*) Snapshots of density field for $t = 28.610, 28.614, 28.618, 28.626$ s. (*b*) Pressure fields for the same timings. (*c*) Pressure-time series for points A, . . . , D, as marked in the snapshots. (*d*) Pressure at wall in the (t, y)-plane with the pressure scale identical to that of the plots in (*b*). Time instants of the snapshots are marked by solid vertical lines in (*c*, *d*). The dotted vertical lines in (*d*) indicate the time interval for integration of impulse; see § 5.5.

the same fashion as in figure 13, while the surface profile of the incompressible-flow computation is plotted on top as a black line. The two solutions are seen to be in good agreement away from the wall. In the impact zone, the jet forms later in the compressible solution than in the potential-flow solution. This is probably due to the combined effect of the slower velocity at which pressures propagate, the presence of air outside the water phase and numerical damping. Pressure-time series from the compressible and incompressible computations are compared in § 5.5.

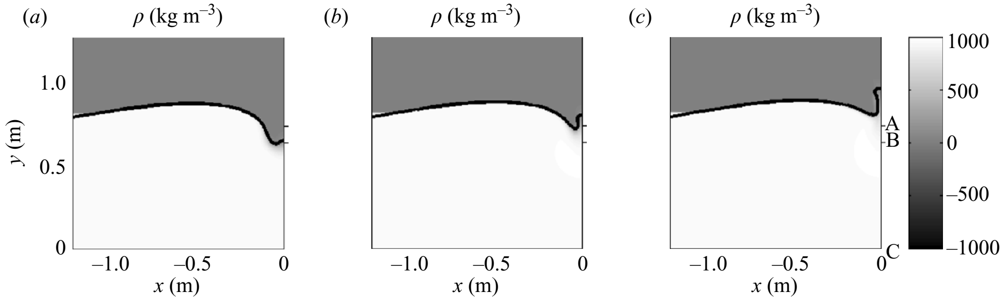

FIGURE 14. Comparison of the density field from the compressible-flow computation with the surface profile from the incompressible computation for $t = 28.610, 28.614, 28.618$ s.

5.3. *Impact with a small air pocket (compressible computations)*

Results for $H = 1.45$ m are shown in figures 15–16. Although the offshore wave height is only 0.09 m greater than that of the previous example, the first two columns of figure 15 clearly show that the 1.45 m wave overturns just before it reaches the wall and traps a small pocket of air. This gives rise to pressures that reach 54.2 ρgh inside the air pocket in the vicinity of point B, marked at the right edge of the frames. The last two columns of the figure show the air pocket beginning to move up the wall, while the flow of aerated water around the top of the pocket forms an upward jet. As before, high pressures propagate away from the impact zone. The time series in figure 15(*c*) show that the crest of the pressure wave has just passed point C by the time of the fourth set of snapshots.

The further evolution of the pressure wave is presented in figure 16, where it can be seen that the front of the wave retains its semicircular shape and develops into a shock wave. The sudden increase in pressure associated with the passage of this wave is apparent both in the pressure snapshots of the first and second columns and in the (t, y)-plot in the lower panel. The lower edge of the shock wave becomes progressively steeper as the wave propagates down towards the mound at an estimated speed of 80 m s^{-1}. Because reflection accentuates the pressure differential, there is an even more dramatic jump in pressure when the wave is reflected. This is well illustrated by the pressure record for point D at the toe of the wall and in the lower panel. After reflection, the wave starts to propagate back up the wall while still extending further seawards across the mound, as indicated by the last two columns of snapshots in figure 16. Once this compression wave reaches the free surface, it undergoes a negative reflection and a rarefaction wave returns back towards the mound.

The pressure-time series for points A and B on the wall show that pressures in the impact zone become sub-atmospheric ($p - p_0 < 0$) around 8 ms after the impact. This is caused by the expansion of the trapped air following its initial violent compression. Over-expansion of the air pocket is followed by recompression, up to about 13 ρgh by $t = 28.49$ s at point B, leading to an oscillatory variation in pressure that gradually dies away. Both the sub-atmospheric pressure and the pulsation are visible in the (t, y) pressure plot. The pulsation causes a secondary pressure wave to be radiated away from the impact zone. The snapshot in the fourth column of figure 16, together with the (t, y)-plot in the lower panel, clearly shows the propagation of this wave down the wall. On the way down, it interacts with the reflected wave from the first pressure peak that is coming up the wall. This indicates that for wave impacts with

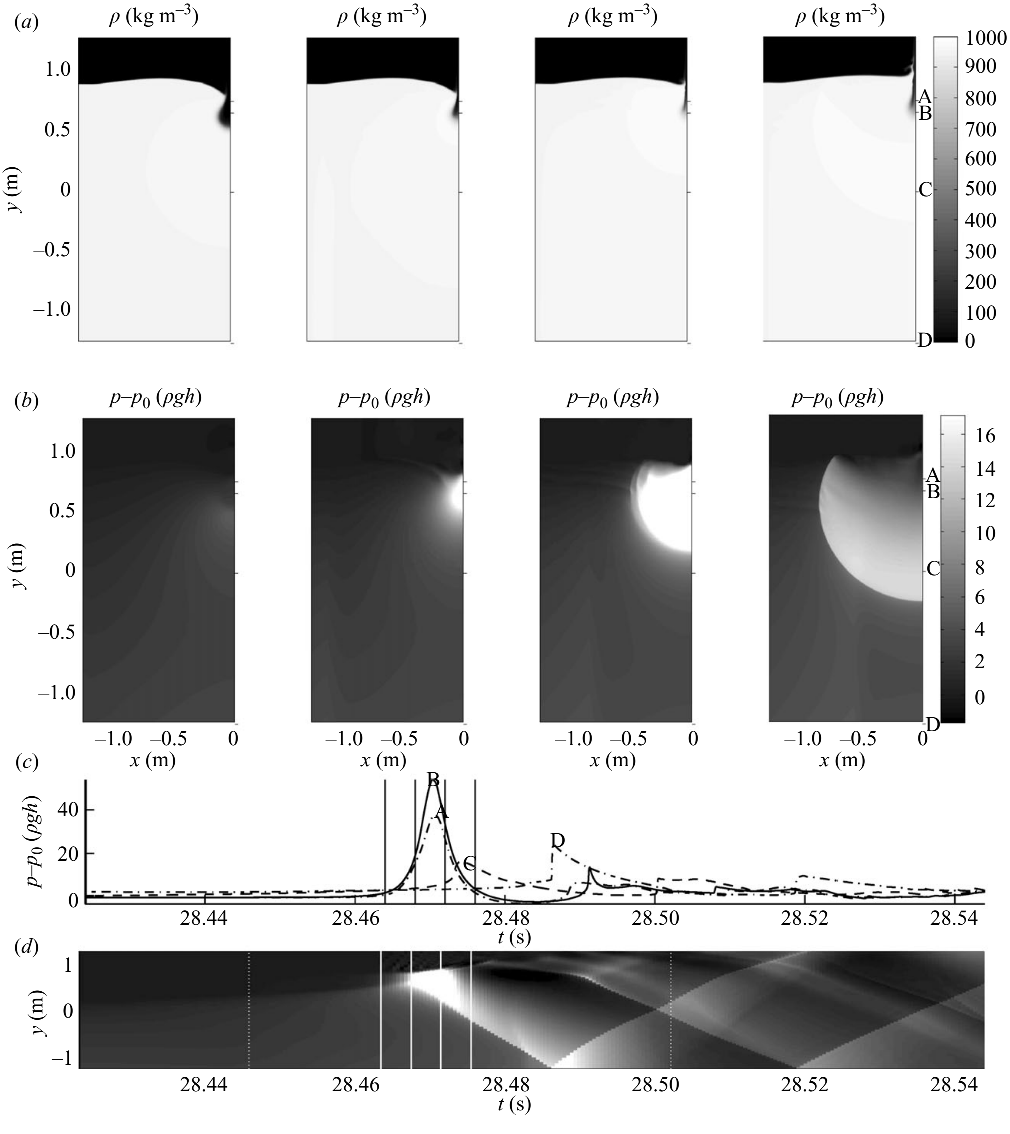

FIGURE 15. Density and pressure variation during an impact that traps a small air pocket. $H = 1.45$ m. See caption of figure 13 for explanation of figure layout. Timings of snapshots are $t = 28.464, 28.468, 28.472, 28.476$ s.

trapped air pockets, at least two mechanisms can lead to the recurrence of high pressures in the impact zone. One is the reflection by both the mound and the free surface that leads to the propagation of pressure waves up and down the wall. The other is the pulsation of the trapped air. Bullock *et al.* (2007) used their experimental measurements of sub-atmospheric and oscillatory pressures in the impact zone, similar to those described above, to help identify high-aeration wave impacts where air entrapment was suspected. Physical records of this type have already been presented in figure 2(*c*).

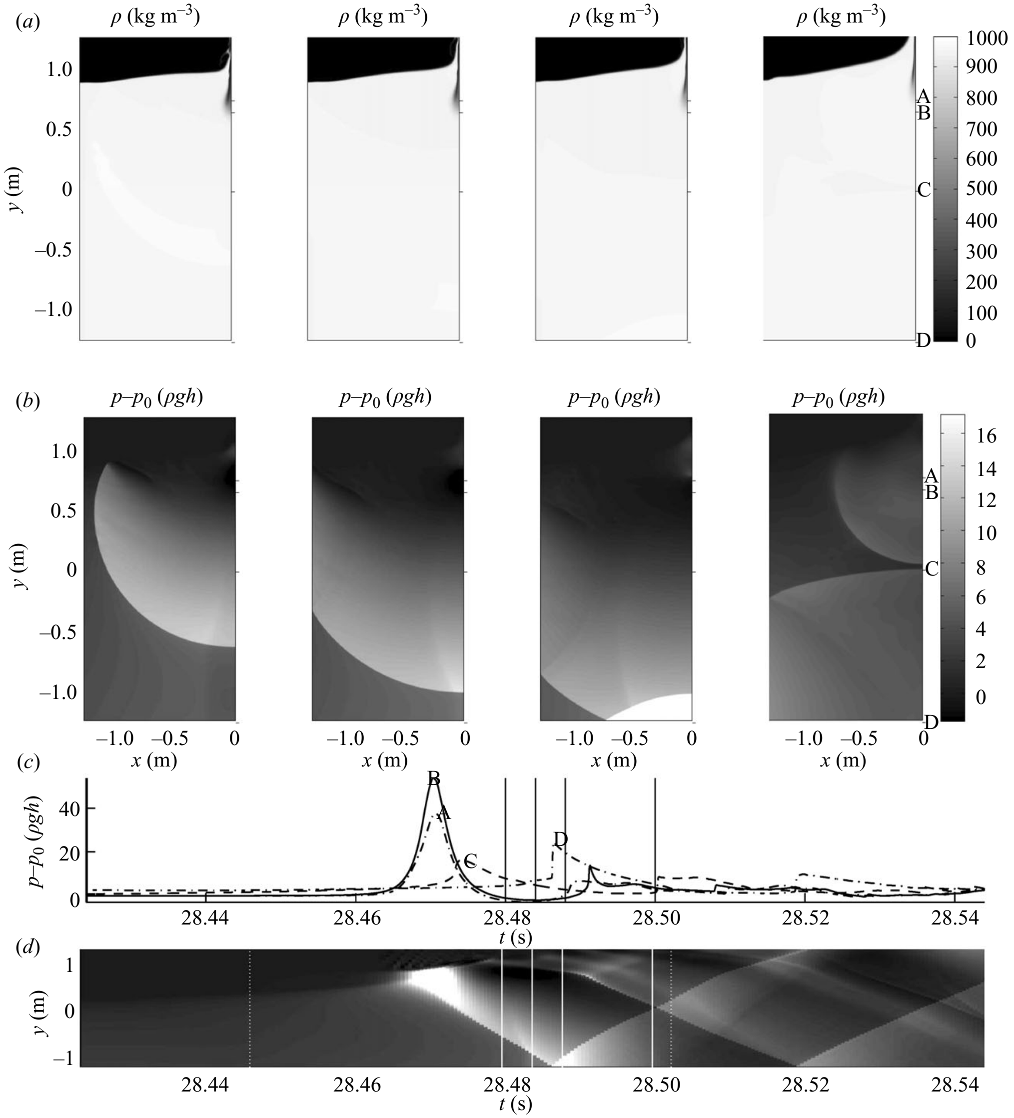

FIGURE 16. Density and pressure variation during an impact that traps a small air pocket. $H = 1.45$ m. See caption of figure 13 for explanation of figure layout. Timings of snapshots are $t = 28.480, 28.484, 28.488, 28.500$ s.

5.4. *Impact with a larger air pocket (compressible computations)*

Results for $H = 1.48$ m are shown in figures 17 and 18. The trapped air pocket for this impact is slightly larger than that for the 1.45 m wave due to the more pronounced overturning of the breaker. The snapshots of the density field in figure 17 show how a tongue of water from the wave crest hits the wall, traps the air and is deflected into a vertical jet. Shortly afterwards, the air in the pocket reaches a maximum pressure of 29.4 ρgh. Once again, a pressure wave similar to those discussed previously propagates away from the impact zone and reflects from the top of the mound. However, this time the pressure wave is not strong enough to develop into a shock wave. Conversely, the oscillatory pressures associated with the pulsation of the larger trapped air pocket

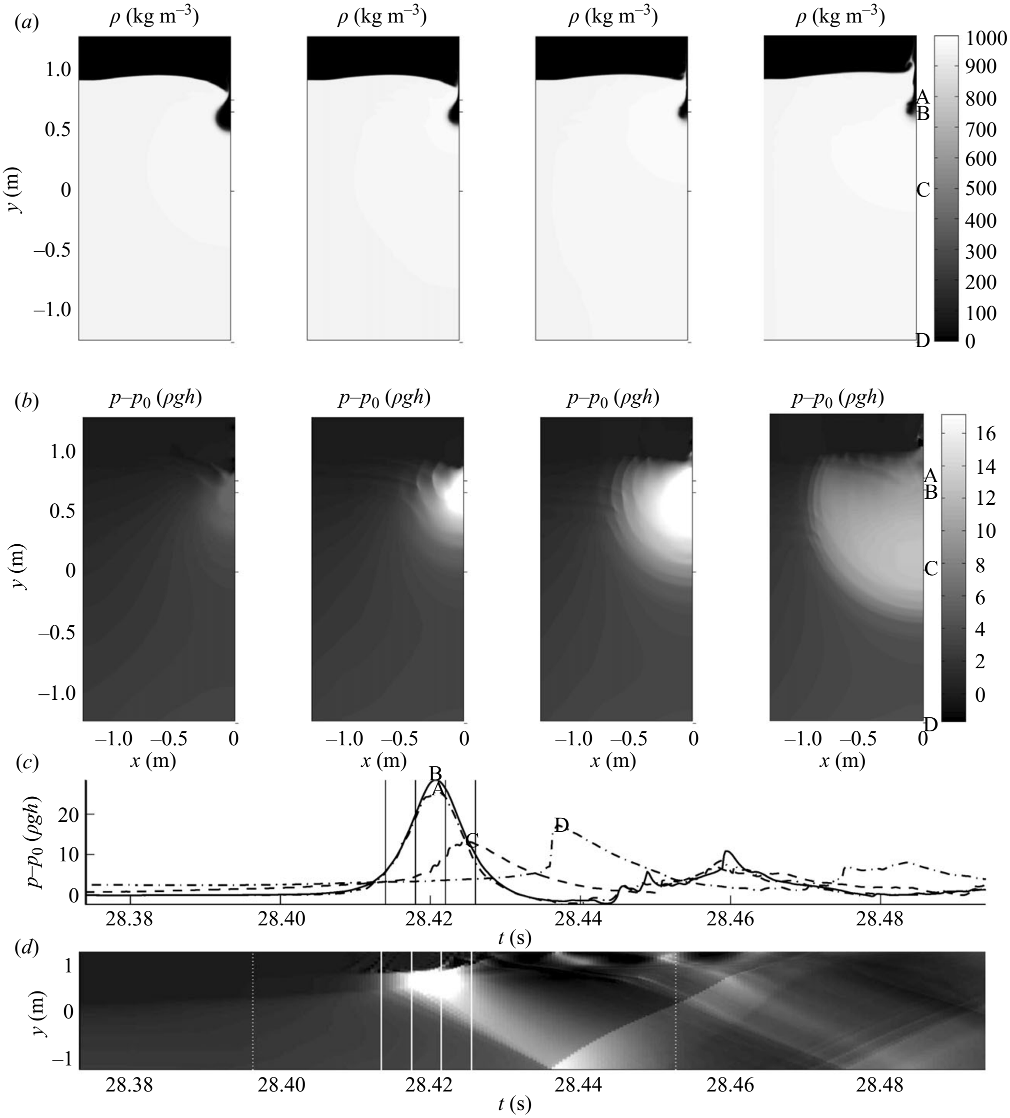

FIGURE 17. Density and pressure variation during an impact that traps a larger air pocket. $H = 1.48$ m. See caption of figure 13 for the explanation of figure layout. Timings of snapshots are $t = 28.414, 28.418, 28.422, 28.426$ s.

are more pronounced than in the previous example, as can be seen in the lower panels of figures 17–18 for points A and B.

5.5. *Pressures, forces and impulse (compressible computations)*

The compressible computations enable impact pressures and forces to be studied for wave heights larger than the one associated with the limiting flip-through case. Figure 19 shows the variation of wall pressure for impacts of waves with different offshore heights. Each curve is for the point on the wall where the maximum pressure occurred during that event. All the computations were carried out in the same way as the examples described previously. The maximum pressures are listed in table 1.

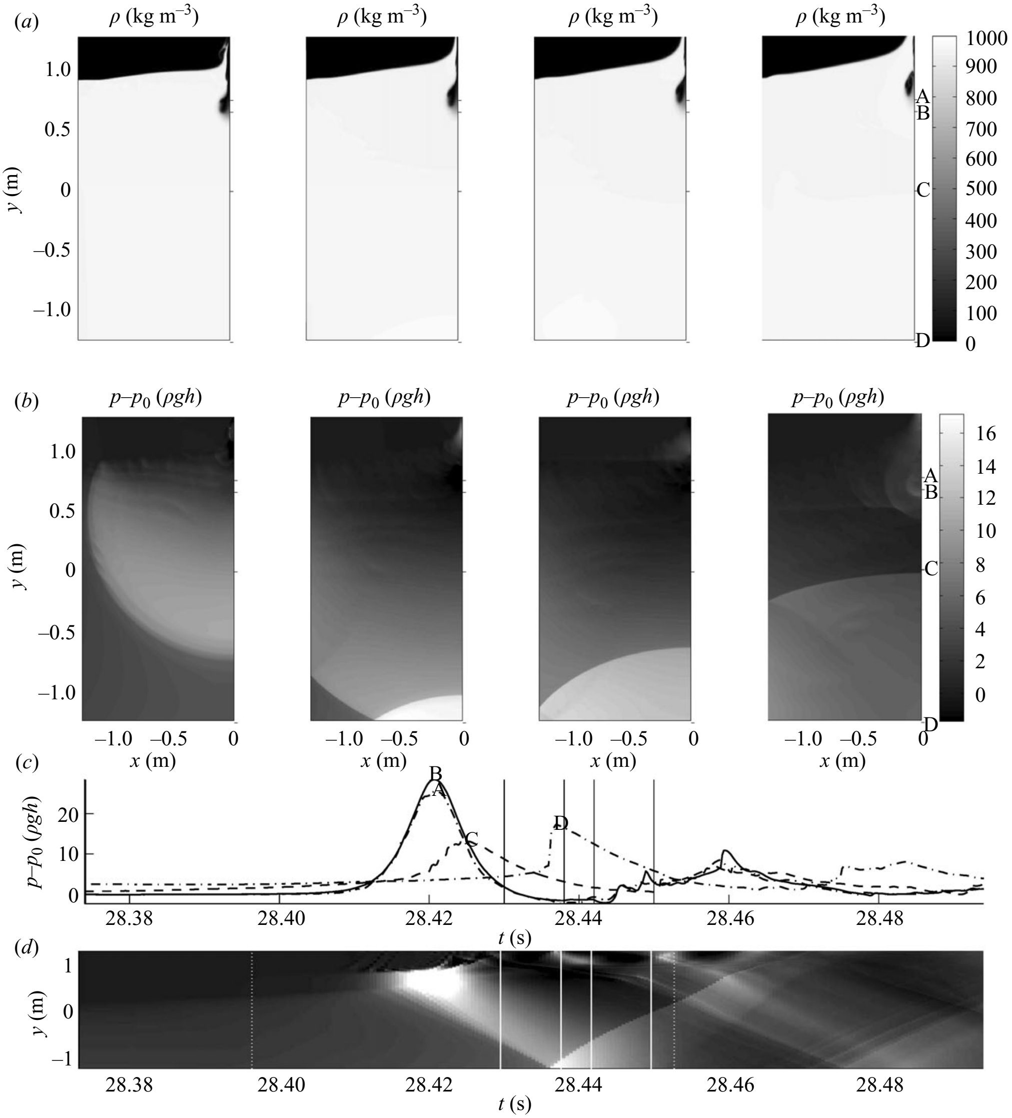

FIGURE 18. Density and pressure variation during an impact that traps a larger air pocket. $H = 1.48$ m. See caption of figure 13 for the explanation of figure layout. Timings of snapshots are $t = 28.430, 28.438, 28.442, 28.450$ s.

The data indicate that the maximum impact pressure increases with increasing offshore wave height until it reaches 54.2 $\rho g h$ at $H = 1.45$ m for the wave that traps a small air pocket, as shown in figures 15 and 16. Further increase in the offshore wave height then causes the maximum impact pressure to decrease as progressively more air is trapped. This is in line with the observations of Bagnold (1939) and Hattori *et al.* (1994), who found that the largest impact pressures occurred with waves that trapped a small amount of air. The impact pressures associated with the high-aeration events also tend to have longer rise times and durations than the low-aeration events, in accordance with the GWK data (Bullock *et al.* 2007).

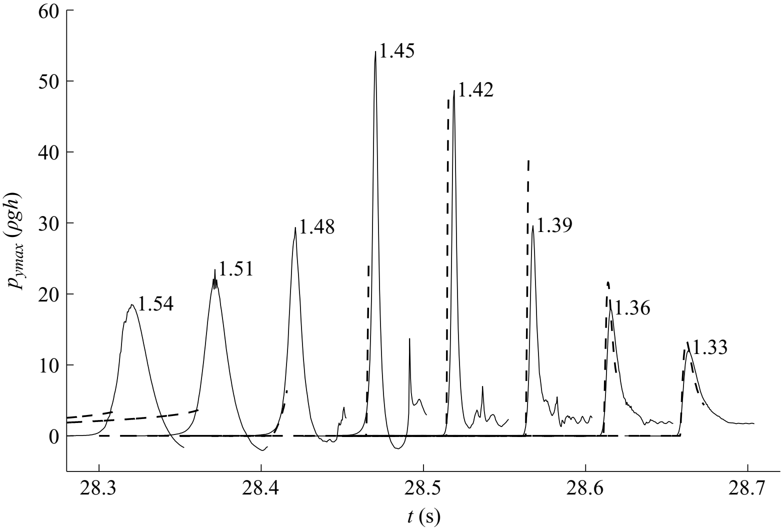

FIGURE 19. Pressure variation on the wall predicted by the compressible model (solid lines) for the location experiencing the highest pressure. Each curve is labelled with the value of H in metres. Results from the incompressible-flow computations are shown by dashed lines.

H (m)	$p_{max} - p_0$ (ρgh)	F_{max} (ρgh^2)	Impulse ($\rho gh^2(h/g)^{1/2}$)
1.33	12.0	8.53	1.04
1.36	17.9	10.0	1.12
1.39	29.6	12.7	1.29
1.42	48.7	17.2	1.29
1.45	54.2	21.2	1.32
1.48	29.4	18.4	1.30
1.51	23.5	18.8	1.52
1.54	18.5	18.3	1.71

TABLE 1. Maximum pressure, maximum force and impulse for various offshore wave heights obtained from the compressible computations.

Pressure-time series from the incompressible-flow computations are also reproduced in figure 19. Each curve is for the point on the wall at which the highest pressure occurs in that particular computation. Note that the vertical position of this point not only varies with H, it may also be different between compressible and incompressible results obtained for the same value of H.

A direct comparison of the maximum pressures can be made for only the two smallest wave heights. In both cases, the compressible model predicts lower maximum pressures, with reductions of 10 % for $H = 1.33$ m and 17 % for $H = 1.36$ m. This is attributed to the cushioning effect of the air flow prior to impact, the compressibility of the aerated water phase caused by the initial uniform aeration of 5 % and numerical grid effects. By the time they break down, the pressures of the incompressible computation for $H = 1.39$ m already exceed the maximum reached by the compressible computation. For $H = 1.42$ m the break down occurs at a pressure similar to the maximum pressure of the compressible computation.

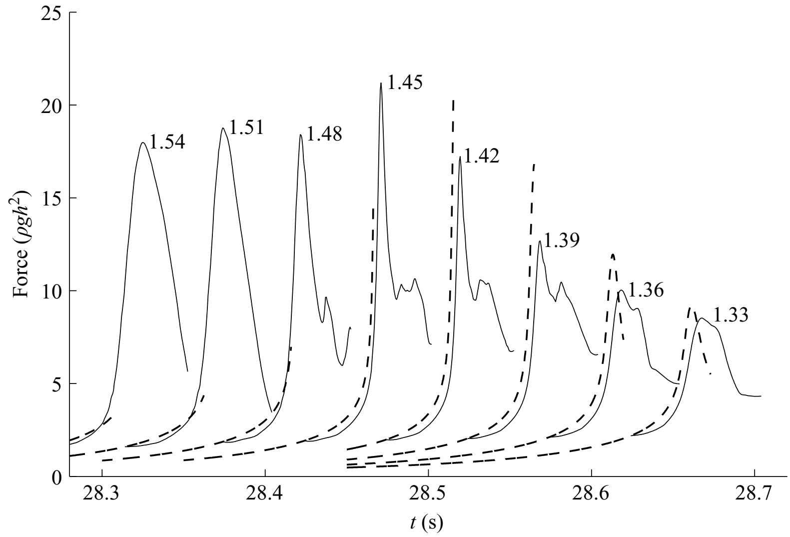

FIGURE 20. Force on the wall predicted by the compressible model (solid lines). Each curve is labelled with the value of H in metres. Results from the incompressible-flow computations are shown by dashed lines.

The instantaneous force on the wall from the compressible computations can be obtained by vertical integration of the pressure field. The results are shown in figure 20 and the maximum values are summarized in table 1. Like the maximum pressure, the maximum force increases with the offshore wave height up to $H = 1.45$ m. Here it reaches a maximum of 21.2 ρgh^2, which is 42 times the hydrostatic force associated with still water, and significant pulsations occur after the main peak. However, unlike the maximum pressures, the maximum force does not decrease rapidly when the wave height is further increased. This is largely due to the fact that the high-pressure region increases with the size of the air pocket and lends support to the observation of Bullock *et al.* (2007) that, even when the pressures during a high-aeration impact are lower, the fact that the impact is generally less spatially localized than a low-aeration impact reduces the chance of the resultant force being lower.

Forces for the incompressible computations are shown in the figure by dashed lines. For the two smallest wave heights, the maximum forces predicted by the compressible computations are 7 % and 16 % lower than for their incompressible counterparts. However, the compressible peak forces last for a longer duration. These differences are in part caused by the fact that in the compressible computations, such as that illustrated in figure 13, the maximum pressures do not occur simultaneously at all elevations on the wall, whereas in the incompressible computations, such as that illustrated in figure 12, they do. For impacts that trap an air pocket, yet another effect adds to the duration of the force peak as illustrated in figures 15 and 17, where the high-impact pressures are clearly associated with the compression of trapped air. In this situation, the duration of the force contribution from the air is governed by the dynamics of the air pocket, which for the computations presented has a longer time scale than the pressures associated with low-aeration events. This helps to explain why high-aeration impacts tend to have a longer duration than low-aeration impacts.

While the extreme pressures associated with violent impacts can be expected to be responsible for local damage, such as the removal of blocks from a masonry breakwater (Müller *et al.* 2002; Wolters *et al.* 2004), the resultant force and its impulse are likely to be more important as far as the overall stability of a structure is concerned. For the purposes of this study, we define the following ad hoc measure for the impulse for the compressible computations:

$$I = \int_{t_1}^{t_2} F(t)\,\mathrm{d}t \tag{5.1}$$

with t_1 and t_2 chosen on the basis of the following relationships:

$$t_1 = t_{max} - 1.5(t_{bot} - t_{max}), \tag{5.2}$$

$$t_2 = t_{bot} + 1.0(t_{bot} - t_{max}), \tag{5.3}$$

where t_{max} is the time of maximum pressure and t_{bot} is the time of maximum pressure at the foot of the wall. Although the limits are somewhat arbitrary, they ensure that most of the rise time to maximum pressure as well as the contribution from the pressure wave going down and up the wall contributes to the impulse. The computed values of t_1 and t_2 are marked with dotted lines in figures 13(*d*) and 15(*d*)–18(*d*). Clearly, the impulse measure (5.1) is associated with the initial 'impact pressure' of the impacts as defined in § 2. The values of the impulses calculated on this basis for each of the offshore wave heights are listed in table 1. The results indicate that the impulse increases monotonically with the wave height over the range covered. Above $H = 1.45$ m, the increase in the impulse is mainly due to the tendency for the duration of the force peak to increase with the size of the trapped air pocket as indicated by figure 20. This is in agreement with Wood, Peregrine & Bruce (2000), who showed that the presence of trapped air can act to increase the pressure impulse for wave impacts, and Bullock *et al.* (2007), who concluded that the impulse due to a high-aeration impact could well be higher than that due to a low-aeration impact.

6. Summary and discussion

Attention has been drawn to the complex role of air in violent breaking-wave impacts. Such impacts generally occur at times when previous events have already caused a substantial volume of air to be entrained in the water and further air may well be trapped between the wave and the structure against which it breaks. In order to gain a greater understanding of the processes involved, a numerical study of aerated violent wave impacts has been carried out by an incompressible potential-flow model and a novel compressible-flow model that accommodates both entrained and trapped air.

The compressible model is based on conservation equations for mass, momentum, air mass and energy and is solved in a finite-volume framework, with no assumption of smooth flow. An exact Riemann solver for the model equations has been developed and the model has been successfully validated for a one-dimensional test case based on a piston system. One-dimensional tests of shock wave propagation from air into water have shown that the numerical smearing that inevitably occurs at such an interface may lead to spurious oscillations at the front of the transmitted wave. A sufficiently refined numerical mesh must be used to keep the oscillations under control.

The models have been applied to waves of varying offshore height breaking against a vertical wall in a two-dimensional situation similar to that investigated physically in the GWK (Bullock *et al.* 2007). Results from the incompressible-flow model give insight into which type of impact is likely to occur and have been used to provide initial data and boundary conditions for the new compressible-flow model that accommodates both entrained and trapped air. Detailed computations have been presented for aerated wave impacts of the flip-through type through to overturning. The results show that the compressible model can successfully reproduce all of the main characteristics of violent breaking-wave impacts observed in the GWK tests (Bullock *et al.* 2007) and provide new insights into the physics of the processes involved. Phenomena reproduced include:

- Strong sensitivity of maximum impact pressures to wave conditions.
- The association of the highest impact pressures with the entrapment of small pockets of air, in accordance with the classic observations of Bagnold (1939) and Hattori *et al.* (1994).
- Very high pressures in the impact zone (up to 54.2 $\rho g h$ in the present computations) which may cause localized damage to the structure.
- Oscillatory pressures and forces associated with the alternate compression and expansion of trapped air pockets. In the more extreme cases, pressures can become sub-atmospheric, leading to the generation of potentially destabilizing seaward forces on parts of the structure.
- Pressure waves that develop into shock waves in the more extreme circumstances.
- High pressures at the toe of the structure due to pressure waves propagating down from the impact zone being reflected from the top of the mound. Such pressures could potentially destabilize the bed material, the structure or both.
- The possible increase in the magnitude of impact forces and impulses by the entrapment of air due to the increase in the spatial and temporal extent of the impact zone even though the presence of air may reduce the magnitude of the maximum pressure.

The results of the present paper have focused mainly on how the incident wave height influences the impact type and pressure variation. The successful development of a compressible model that reproduces the main features of physical wave impacts, however, opens up many other possible areas for study. For example, the effect of other levels of initial aeration could be investigated in addition to the uniform 5 % level considered here. This could include more realistic scenarios in which the initial aeration was non-uniform and designed to represent the cloud of bubbles close to the wall entrained by a previous impact. A range of practical problems could also be investigated. Possibilities include the way in which the wave-induced forces could be reduced by making changes to the structural geometry, the response of structures to dynamic loading and the displacement of bed material by the pressure waves that propagate offshore. The compressible model is also particularly well suited to the study of scale effects in small-scale hydraulic model investigations. Indeed, a start on this has already been made (Bredmose & Bullock 2008). It should also be noted that the application of the compressible-flow model is not limited to wave impacts on coastal structures. It may just as well be applied to impacts on offshore structures, ships or to the study of sloshing inside LNG tanks within ships.

Although the results presented here successfully reproduce the main characteristics of the experimental observations, they are naturally limited by their inherent assumption of a two-dimensional flow. Among the relevant three-dimensional effects that are thereby precluded in the modelling is the crossflow non-uniformity of the impacting wavefront that is likely to affect the dynamics of the air pocket. In this situation, air leakage may therefore take place in the sideways direction as well as through the gap between the wavefront and the wall. This non-uniformity in the air flow is likely to affect the propagation of pressure sound waves, while the three-dimensional turbulence field along the wavefront may also affect the loads on the wall. The propagation of sound waves from an oscillating air pocket and its subsequent collapse is discussed by Colicchio *et al.* (2007). An extension of the present analysis and computation to three dimensions would be relatively straightforward, although the demands on CPU and computational memory would increase to a great extent. Such computations are a natural next step from the present study, as it could lead to an even more realistic representation of the behaviour of trapped air by taking crossflow non-uniformity and the associated effect on pressure wave propagation into account. This could introduce the three-dimensional variability of impact pressures seen in supposedly two-dimensional laboratory tests and further would increase the potential application of the model to three-dimensional flows where the role of compressibility is important.

The work was mainly supported by the UK Engineering and Physical Sciences Research Council (grants GR/R29772/01, EP/C515072/1 and GR/R29789/01). Additional support was provided by the EU Transnational Access To Major Research Infrastructure activity for the tests in the GWK which were carried out in collaboration with Dipl-Ing. J. Grüne and Dr G. Müller and conducted by Dr C. Obhrai and Dr G. Wolters. Prof. R. LeVeque is thanked for valuable inputs on the numerical solution of the aerated-flow model. Dr A. Hogg proof read the manuscript and is thanked for many useful comments. The paper is dedicated to Prof. Howell Peregrine, who initiated and guided this aspect of the BWIMCOST research. The work presented here is a direct outcome of his enthusiasm and dedication to fluid mechanics and free surface flows. He passed away while the manuscript was at an early stage. The remaining authors are grateful for his inspiration and the many stimulating discussions they had with Howell over the years.

Appendix A. Energy conservation for isentropic flow

When no shock waves are present, the flow is isentropic and the energy conservation equation (3.8*e*) can be replaced by the direct use of the pressure relation (3.3). In this case, energy conservation follows directly from conservation of mass, momentum and gas mass in combination with (3.3). Here, we show that for smooth flows, these two formulations are equivalent. The implication of this is that while the energy conservation equation ensures a correct modelling of shock waves, it does not alter the smooth solutions of the system for isentropic flow.

The task is thus to show that (3.8*e*) with the energy density defined by (3.7) is identically satisfied for smooth flows that satisfy (3.8*a*)–(3.8*d*), (3.2) and (3.3).

We first write the energy conservation equation as

$$\mathscr{E} = E_t + [(E+p)u]_x + [(E+p)v]_y + \rho g v = 0. \tag{A 1}$$

For the first term, we find

$$E_t = \frac{(\beta p)_t}{\gamma - 1} + \frac{1}{2}\left(\frac{(\rho u)^2}{\rho}\right)_t + \frac{1}{2}\left(\frac{(\rho v)^2}{\rho}\right)_t = \frac{(\beta p)_t}{\gamma - 1} + u(\rho u)_t - \frac{1}{2}u^2\rho_t + v(\rho v)_t - \frac{1}{2}v^2\rho_t.$$

The time derivatives of ρ, (ρu) and (ρv) are substituted from the mass and momentum equations (3.8*a*)–(3.8*c*). After algebraic reduction, we obtain

$$
\begin{aligned}
E_t = {} & \frac{(\beta p)_t}{\gamma - 1} - u\left(\frac{1}{2}\rho u^2 + p\right)_x - v\left(\frac{1}{2}\rho v^2 + p\right)_y - \rho v g \\
& -\tfrac{1}{2}\rho u^2 u_x - \tfrac{1}{2}\rho_y u^2 v - \rho u v u_y - \tfrac{1}{2}\rho u^2 v_y \\
& -\tfrac{1}{2}\rho_x u v^2 - \tfrac{1}{2}\rho v^2 u_x - \rho u v v_x - \tfrac{1}{2}\rho v^2 v_y.
\end{aligned}
\tag{A 2}
$$

The next terms in (A 1) are obtained by direct differentiation, leading to

$$
\begin{aligned}
[(E + p)u]_x = {} & \frac{1}{\gamma - 1}\beta u p_x + \frac{1}{\gamma - 1}(\beta u)_x p + p u_x \\
& + u\left(\tfrac{1}{2}\rho u^2 + p\right)_x + \tfrac{1}{2}\rho u^2 u_x + \tfrac{1}{2}\rho_x u v^2 + \tfrac{1}{2}\rho u_x v^2 + \rho u v v_x,
\end{aligned}
\tag{A 3}
$$

$$
\begin{aligned}
[(E + p)v]_y = {} & \frac{1}{\gamma - 1}\beta v p_y + \frac{1}{\gamma - 1}(\beta v)_y p + p v_y \\
& + v\left(\tfrac{1}{2}\rho v^2 + p\right)_y + \tfrac{1}{2}\rho v^2 v_y + \tfrac{1}{2}\rho_y u^2 v + \tfrac{1}{2}\rho u^2 v_y + \rho u v u_y.
\end{aligned}
\tag{A 4}
$$

The insertion of (A 2)–(A 4) into (A 1) gives after algebraic reduction

$$
\begin{aligned}
\mathscr{E} = {} & \frac{\beta_t p}{\gamma - 1} + \frac{\beta p_t}{\gamma - 1} + \frac{1}{\gamma - 1}(\beta u)_x p + p u_x + \frac{1}{\gamma - 1} p_x u \beta \\
& + \frac{1}{\gamma - 1}(\beta v)_y p + p v_y + \frac{1}{\gamma - 1} p_y v \beta.
\end{aligned}
\tag{A 5}
$$

The differentiation of the pressure relation (3.3) gives

$$
p_\xi = p_0 \gamma \left(\frac{\sigma}{\sigma_0}\right)^{\gamma - 1} \frac{\sigma_\xi}{\sigma_0} = \gamma \frac{p}{\sigma} \sigma_\xi,
\tag{A 6}
$$

where ξ can be x, y or t. Insertion into (A 5) yields after subtraction of $\gamma p / ((\gamma - 1)\sigma)$ times (3.8*d*)

$$
\mathscr{E} = p[-\beta_t + (1 - \beta)u_x - u\beta_x + (1 - \beta)v_y - v\beta_y].
\tag{A 7}
$$

The last step is to introduce the constitutive relation (3.2) into the mass equation (3.8*a*). We obtain

$$
(\beta\sigma)_t - M\beta_t + (\beta\sigma u)_x + [(1 - \beta)Mu]_x + (\beta\sigma v)_y + [(1 - \beta)Mv]_y = 0.
\tag{A 8}
$$

Upon subtraction of (3.8*d*) from this result and division by M we get

$$
-\beta_t + (1 - \beta)u_x - u\beta_x + (1 - \beta)v_y - v\beta_y = 0,
\tag{A 9}
$$

which is identical to the bracket on the right-hand side of (A 7), and thus $\mathscr{E} = 0$.

Appendix B. Grid convergence

The compressible aerated-flow computations of this paper have been carried out on a uniform numerical grid of 500 × 1000 cells (2.5 mm × 2.5 mm). An impression of the grid can be seen in figure 21. Grid convergence has been assessed by comparing the pressure-time histories on the wall at $y = 0.65$ m (point B in figures 13, 15–18) for this grid and for a coarser grid of 250 × 500 cells. Point B is close to the

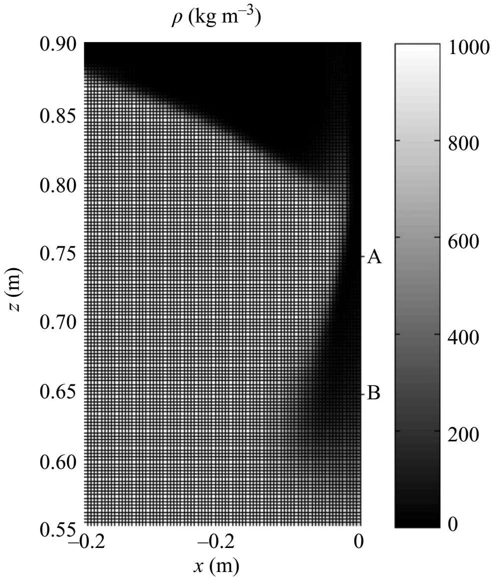

FIGURE 21. Close-up of density field (H = 1.45 m, t = 28.468 s) overlayed with the numerical grid of 500 × 1000 cells. The full spatial extent of the density field can be seen in the second column of figure 15.

H (m)	$p_{peak} - p_0$ 250 × 500 ($\rho g h$)	$p_{peak} - p_0$ 500 × 1000 ($\rho g h$)
1.33	11.4	12.0
1.45	37.0	53.8
1.54	16.7	17.8

TABLE 2. Peak pressures in y = 0.65 m computed at different grids.

point of maximum pressure for all of the impacts covered by these figures. The resultant pressure-time series for wave heights of 1.33 m, 1.45 m and 1.54 m are shown in figure 22 while the peak pressures are listed in table 2. For $H = 1.33$ m and H = 1.54 m, the application of the coarse grids leads to a reduction in peak pressure of 4.9 % and 6.1 %, respectively. For H = 1.45 m the reduction is 31 % and clearly indicates that for this wave height, full convergence for the peak pressure has not been achieved. An additional computation, shown as a dotted line in figure 22(*b*), using an intermediate grid of 400 × 800 cells confirms this finding as a peak pressure of 47.6 $\rho g h$ was achieved. This is 12 % smaller than peak pressure obtained with the 500 × 1000 cell grid.

The real maximum pressures during impact are thus likely to be even higher than computed here for the most violent impacts. The associated need for high numerical resolution can be linked to the flow behaviour at the time where the maximum pressure occurs; see columns 2 and 3 of figure 15. The largest pressure in point B occurs when a small upward jet is formed at the bottom edge of the trapped air pocket. This jet is small in size and is formed from air–water mixture with intermediate density. Coarsening the grid leads to poorer resolution of the jet and is also likely to

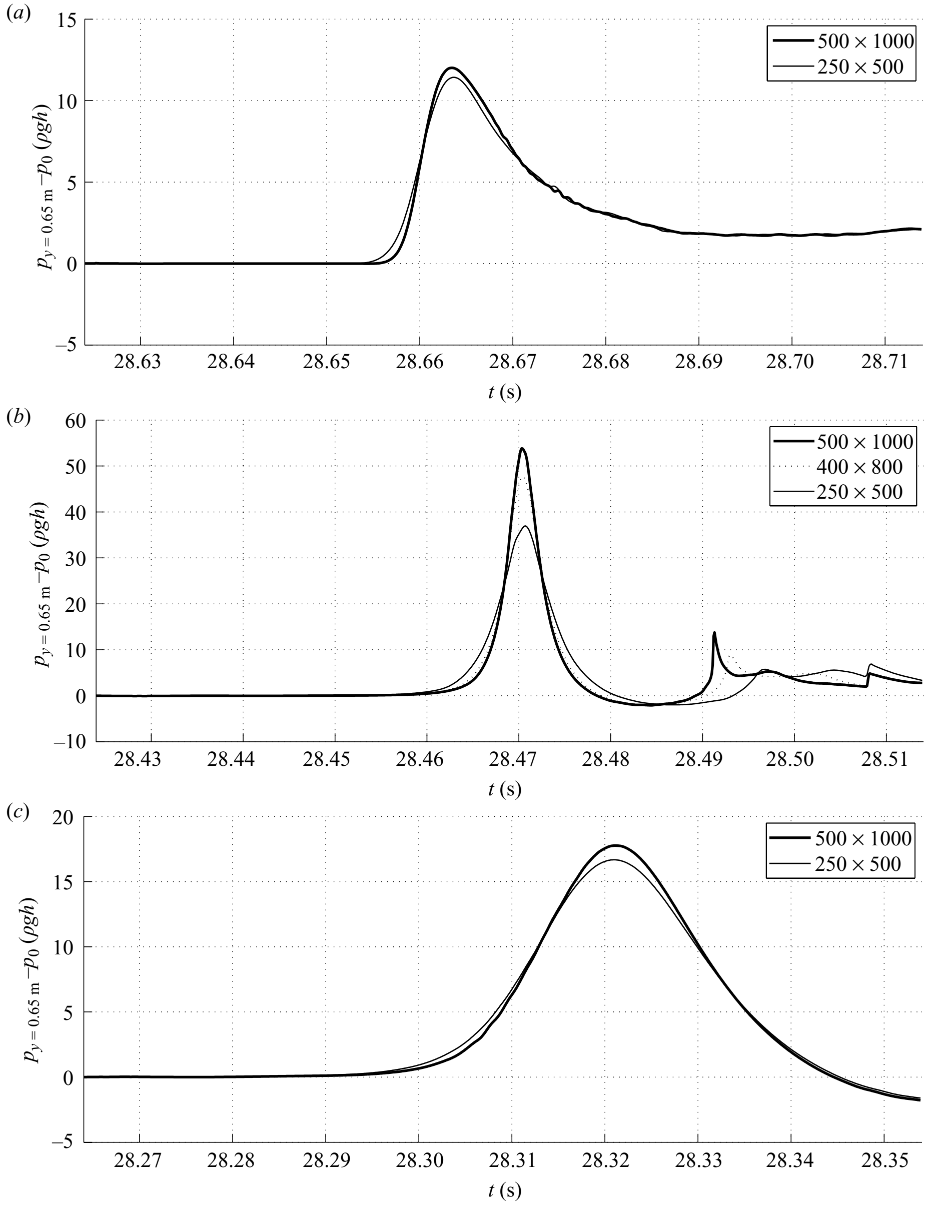

FIGURE 22. Time series for pressure in $y = 0.65\,\mathrm{m}$ computed at different grids. (*a*) is for $H = 1.33\,\mathrm{m}$, (*b*) for $H = 1.45\,\mathrm{m}$ and (*c*) for $H = 1.54\,\mathrm{m}$.

increase the thickness of the air–water interface at the bottom of the pocket. This in turn affects the pressures due to the dependence of sound speed to aeration level.

The above results indicate that the converged peak pressures for the most violent impacts are even higher than those obtained in this study on the 500 × 1000 cell grid. An analysis of the results from the coarse grid computations, however, leads to the same qualitative variation with respect to wave height for maximum pressure and force, while the results for impulse are nearly identical between the two grids.

One computation with 500×1000 cell resolution typically took approximately 3 days on a 2.6 GHz AMD Opteron CPU and a doubling of the resolution implies that the CPU time would increase by a factor of eight. This is due to the associated increase in the number of computational cells by a factor of four combined with the doubling of the number of time steps. Computations using a 1000×2000 cell grid were therefore considered impractical. Ongoing work in this regard is the introduction of adaptive grid refinement that allows a local and dynamic improvement of grid resolution and development of an approximate Riemann solver that avoids the iterative solution of a nonlinear scalar equation for each Riemann problem.

REFERENCES

Bagnold, R. A. 1939 Interim report on wave-pressure research. *Proc. Inst, Civil Engng* **12**, 201–226.

Bird, P. A. D., Crawford, A. R., Hewson, P. J. & Bullock, G. N. 1998 An instrument for field measurement of wave impact pressures and seawater aeration. *Coastal Engng* **35**, 103–122.

Blackmore, P. A. & Hewson, P. J. 1984 Experiments on full-scale wave impact pressures. *Coastal Engng* **8**, 331–346.

Bredmose, H., Brocchini, M., Peregrine, D. H. & Thais, L. 2003 Experimental and numerical investigation of steep forced water waves. *J. Fluid Mech.* **490**, 217–249.

Bredmose, H. & Bullock, G. N. 2008 Scaling of wave impact pressures in trapped air pockets. In *Proc. 23rd Intl Workshop on Water Waves and Floating Bodies*. Jeju, Korea.

Bredmose, H., Peregrine, D. H., Bullock, G. N., Obhrai, C., Müller, G. & Wolters, G. 2004 Extreme wave impact pressures and the effect of aeration. In *Proc. 19th Intl Workshop on Water Waves and Floating Bodies*. Cortona, Italy.

Bullock, G. N., Crawford, A. R., Hewson, P. J., Walkden, M. J. A. & Bird, P. A. D. 2001 The influence of air and scale on wave impact pressures. *Coastal Engng* **42**, 291–312.

Bullock, G., Obhrai, C., Müller, G., Wolters, G., Peregrine, D. H. & Bredmose, H. 2003 Field and laboratory measurements of wave impacts. In *Proc. 3rd Coastal Structures Conf*. ASCE.

Bullock, G., Obhrai, C., Müller, G., Wolters, G., Peregrine, D. H. & Bredmose, H. 2004 Characteristics and design implications of breaking wave impacts. In *Proc. 29th Intl Conf. Coastal Engng.* (ed. J. McKee-Smith), pp. 3966–3978. ASCE.

Bullock, G. N., Obhrai, C., Peregrine, D. H. & Bredmose, H. 2007 Violent breaking wave impacts. Part I: Results from large scale regular wave tests on vertical and sloping walls. *Coastal Engng.* **54** (8), 602–617.

Chan, E. S. & Melville, W. K. 1988 Deep-water plunging wave pressures on a vertical plane wall. *Proc. Roy. Soc. Lond.* A **417**, 95–131.

Colicchio, G., Colagrossi, A., Lugni, C., Brocchini, M. & Faltinsen, O. M. 2007 Challenges on the numerical investigation of the flip-through. In *Proc. 9th Intl Conf. Num. Ship Hydrodyn.*, pp. 380–394. CD Rom.

Cooker, M. J. & Peregrine, D. H. 1990 Computation of violent wave motion due to waves breaking against a wall. In *Proc. of the 22nd Intl Conf. Coastal Engng.*, pp. 164–167. ASCE.

Cooker, M. J. & Peregrine, D. H. 1991 Violent motion as near-breaking waves meet a vertical wall. In *Breaking Waves, IUTAM Symp., Sydney 1990* (ed. M. L. Banner & R. H. J. Grimshaw), pp. 291–297. IUTAM, Springer.

Cooker, M. J. & Peregrine, D. H. 1992 Wave impact pressure and its effect upon bodies lying on the sea bed. *Coastal Engng.* **18** (3–4), 205–229.

Cooker, M. J., Vidal, C., Dold, J. W. & Peregrine, D. H. 1990 The interaction between a solitary wave and a submerged semicircular cylinder. *J. Fluid Mech.* **215**, 1–22.

Courant, R. & Friedrichs, K. O. 1948 *Supersonic Flow and Shock Waves*. Interscience.

Dold, J. W. 1992 An efficient surface integral algorithm applied to unsteady gravity waves. *J. Comput. Phys.* **103**, 90–115.

Dold, J. W. & Peregrine, D. H. 1986 An efficient boundary-integral method for steep unsteady water waves. In *Numer. Meth. for Fluid Dynamics II* (ed. K. W. Morton & M. J. Baines), pp. 671–679. Oxford University Press.

Faltinsen, O. M., Landrini, M. & Greco, M. 2004 Slamming in marine applications. *J. Engng Maths.* **48**, 187–271.

Fenton, J. D. 1988 The numerical solution of steady water wave problems. *Computers & Geosciences* **14** (3), 357–368.

Gibson, F. W. 1970 Measurement of the effect of air bubbles on the speed of sound in water. *J. Acoust. Soc. Am.* **48** (5), 1195–1197.

Goda, Y. 2000 *Random Seas and Design of Maritime Structures*. World Scientific.

Godunov, S. K. 1959 A difference method for numerical calculation of discontinuous solutions of the equations of hydrodynamics. *Math. Sbornik.* **47**, 271–306.

Gómez-Gesteira, M. & Dalrymple, R. A. 2004 Using a three-dimensional smoothed particle hydrodynamics method for wave impact on a tall structure. *J. Waterway Port Coastal Ocean Engng* **131** (2), 63–69.

Greco, M., Colicchio, G. & Faltinsen, O. M. 2007 Shipping of water on a two-dimensional structure. Part 2. *J. Fluid Mech.* **581**, 371–399.

Hattori, M., Arami, A. & Yui, T. 1994 Wave impact pressure on vertical walls under breaking waves of various types. *Coastal Engng* **22** (1–2), 79–114.

Hirt, C. W. & Nichols, B. D. 1981 Volume of fluid (vof) method for the dynamics of free boundaries. *J. Comp. Phys.* **39**.

LeVeque, R. J. 2002 *Finite Volume Methods for Hyperbolic Problems*. Cambridge University Press.

Lugni, C., Brocchini, M. & Faltinsen, O. M. 2006 Wave loads: The role of flip-through. *Phys. Fluids* **18** (122101).

McCabe, Anne 2003 The effect of entrained air on violent water wave impacts. PhD thesis, School of Mathematics, University of Bristol.

Müller, G., Hull, P., Allsop, W., Bruce, T., Cooker, M. & Franco, L. 2002 Wave effects on blockwork structures: Model tests. *IAHR J. Hydr. Res.* **40** (2), 117–124.

Nielsen, K. B. & Mayer, S. 2004 Numerical prediction of green water incidents. *Ocean Engng* **31**, 363–399.

Oumeraci, H., Klammer, P. & Partenscky, H. W. 1993 Classification of breaking wave loads on vertical structures. *J. Waterway Port Coastal Ocean Engng.* **119** (4), 381–397.

Oumeraci, H., Kortenhaus, A., Allsop, W., de Groot, M., Crouch, R., Vrijling, H. & Voortman, H. Eds.) 2001 *Probabilistic Design Tools for Vertical Breakwaters*. Hydraulic Aspects, Ch 2. A. A. Balkema.

Partenscky, H. W. 1988 Dynamic forces due to breaking waves on vertical structures. In *Proc. 2nd Intl Symp. Wave Res. Coast. Engng*, pp. 207–220. University of Hannover, Germany.

Peregrine, D. H. 2003 Water wave impact on walls. *Ann. Rev. Fluid Mech.* **35**, 23–43.

Peregrine, D. H., Bredmose, H., Bullock, G., Obhrai, C., Müller, G. & Wolters, G. 2004 Water wave impact on walls and the role of air. In *Proc. 29th Intl Conf. on Coastal Engng, Lisbon 2004*, pp. 4005–4017. ASCE.

Peregrine, D. H., Bredmose, H., Bullock, G. N., Hunt, A. & Obhrai, C. 2006 Water wave impact on walls and the role of air. In *Proc. 30th Intl Conf. Coast. Engng, San Diego* (ed. J. M. Smith), pp. 4494–4506. ASCE.

Peregrine, D. H. & Thais, L. 1996 The effect of entrained air in violent water wave impacts. *J. Fluid Mech.* **325**, 377–397.

Scott, J. C. 1975 The role of salt in white-cap persistence. *Deep Sea Res.* **22**, 653–657.

Scott, J. C. 1976 The preparation of water for surface–clean fluid mechanics. *J. Fluid Mech.* **69**, 339–351.

Slauenwhite, D. E. & Johnson, B. D. 1999 Bubble shattering: Differences in bubble formation in fresh water and seawater. *J. Geophys. Res. Oceans* **104** (C2), 3265–3275.

Tanaka, M., Dold, J. W., Lewy, M. & Peregrine, D. H. 1987 Instability and breaking of a solitary wave. *J. Fluid Mech.* **135**, 235–248.

Tanimoto, K. & Takahashi, S. 1994 Design and construction of caisson breakwaters – the Japanese experience. *Coastal Engng* **22**, 57–77.

Walkden, M. J. A., Crawford, A. R., Bullock, G. N., Hewson, P. J. & Bird, P. A. D 1996 Wave impact loading on vertical structures. In *Advances in Coastal Structures and Breakwaters* (ed. J. E. Clifford), pp. 273–286. Thomas Telford.

Wemmenhove, R. 2008 Numerical prediction of two-phase flow in offshore environments. PhD thesis, Rijksuniversiteit Groningen, The Netherlands.

Wolters, G., Müller, G., Bullock, G., Obhrai, C., Peregrine, D. H. & Bredmose, H. 2004 Field and large scale model tests of wave impact pressure propagation into cracks. In *Proc. 29th Intl Conf. Coast. Engng*, pp. 4027–4039. ASCE.

Wood, D., Peregrine, D. H. & Bruce, T. 2000 Wave impact on a wall using pressure-impulse theory. I: Trapped air. *J. Waterway Port Coastal Ocean Engng* **126** (4), 182–190.

Zhang, S., Yue, D. K. P. & Tanizawa, K. 1996 Simulation of plunging wave impact on a vertical wall. *J. Fluid Mech.* **327**, 221–54.